Influence of Wave Propagation on the Doppler Spreading of Atmospheric Gravity Waves

STEPHEN D. ECKERMANN*

Computational Physics, Inc., Fairfax, Virginia

ABSTRACT

The ''Doppler spread'' theory of atmospheric gravity waves has developed rapidly in recent years, from an initial theory of wave spectra into a general parameterization of gravity wave effects for use in global models of the middle atmosphere. Yet the theory currently employs certain key approximations that have still to be tested. The author focuses on the omission of the propagation of the other waves in the spectrum when determining the Doppler spreading of a given gravity wave. This approximation is shown to become untenable as waves are refracted to progressively shorter vertical scales, so ray methods are employed to investigate the refraction characteristics of short waves within propagating long-wave fields. Short-wave refraction is reduced compared to the Doppler-spread results. While turning levels are common, critical levels do not occur if all waves propagate upward in the absence of mean wind shear. Consequently, a sharp increase in the probability of wave obliteration beyond the so-called cutoff vertical wavenumber (a central tenet of Doppler-spread theory) no longer occurs. Possible implications of these results for models of wave–field interactions, spectra, and momentum deposition are discussed.

1. Introduction

High-resolution probing of the middle atmosphere reveals characteristic vertical wavenumber spectra of gravity wave perturbations of horizontal velocities, temperatures, and densities. In particular, the power spectral densities at vertical scales less than a few kilometers or so are well fitted by a power law of the form $ab(N) M^{-3}$, where M is the Fourier wavenumber, and $b(N)$ depends on the Brunt–Väisälä frequency N and is derived from elementary gravity wave formulas (e.g., see Smith et al. 1987; Tsuda et al. 1991). The scaling factor a is nearly constant, typically around 1/10–1/6, although lower values are sometimes encountered, particularly in the stratosphere (e.g., Hines 1993a; Eckermann 1995).

A number of gravity-wave-based theories have been developed to explain these spectral shapes. Early efforts invoked wave amplitude saturation due to static instabilities as the primary cause (Dewan and Good 1986; Smith et al. 1987). Weinstock (1990) argued that the random fluctuations of saturated small-scale waves produced a diffusive damping of larger-scale waves, and

his theoretical development yielded M^{-3} model spectra [see also subsequent models based on these ideas by Gardner (1994), Zhu (1994), and Medvedev and Klaassen (1995)]. Dewan (1991) derived gravity wave spectra that resembled observations by assuming a cascade of saturated wave energy from larger to smaller spatiotemporal scales. All of these theories arrived at M^{-3} spectra by applying dissipative processes of some kind to the wave field.

An altogether different theory was developed in a series of papers by Hines (1991a,b,c; 1993a,b; 1996; 1997a,b,c), which he has called Doppler-spread theory. While dissipation of wave energy and pseudomomentum are incorporated (e.g., Hines 1997a,b), such processes play no significant role in producing observed spectral shapes within this theory. The Doppler-spread model is most easily introduced by considering a short wave of initial vertical wavenumber m_0 that propagates through a preexisting long wave of vertical wavenumber m_{lw}, such that $|m_{lw}| \ll |m_0|$. In modeling this situation, Doppler-spread theory assumes that the velocity oscillation of the long wave acts like a time-invariant, vertically varying mean-flow profile that refracts the short wave, changing its vertical wavenumber and amplitude as it propagates and thus ''spreading'' its spectral signature through M space. When the long wave is replaced by a spectrum of many randomly phased long waves, their superposed velocity oscillations refract the short wave more randomly. When all waves (both longer and shorter) are considered, Hines (1991a,b) argued that,

---

* Work performed at E. O. Hulburt Center for Space Research, Naval Research Laboratory, Washington, D.C.

Corresponding author address: Stephen Eckermann, E. O. Hulburt Center for Space Research, Code 7641, Naval Research Laboratory, 4555 Overlook Avenue, S.W., Washington, DC, 20375-5320.
E-mail: eckerman@darwin.cpi.com

Report Documentation Page

Form Approved
OMB No. 0704-0188

Public reporting burden for the collection of information is estimated to average 1 hour per response, including the time for reviewing instructions, searching existing data sources, gathering and maintaining the data needed, and completing and reviewing the collection of information. Send comments regarding this burden estimate or any other aspect of this collection of information, including suggestions for reducing this burden, to Washington Headquarters Services, Directorate for Information Operations and Reports, 1215 Jefferson Davis Highway, Suite 1204, Arlington VA 22202-4302. Respondents should be aware that notwithstanding any other provision of law, no person shall be subject to a penalty for failing to comply with a collection of information if it does not display a currently valid OMB control number.

1. REPORT DATE **07 APR 1997**	2. REPORT TYPE	3. DATES COVERED **00-00-1997 to 00-00-1997**

4. TITLE AND SUBTITLE **Influence of Wave Propagation on the Doppler Spreading of Atmospheric Gravity Waves**	5a. CONTRACT NUMBER
	5b. GRANT NUMBER
	5c. PROGRAM ELEMENT NUMBER
6. AUTHOR(S)	5d. PROJECT NUMBER
	5e. TASK NUMBER
	5f. WORK UNIT NUMBER
7. PERFORMING ORGANIZATION NAME(S) AND ADDRESS(ES) **Naval Research Laboratory,E.O. Hulburt Center for Space Research,Washington,DC,20375**	8. PERFORMING ORGANIZATION REPORT NUMBER
9. SPONSORING/MONITORING AGENCY NAME(S) AND ADDRESS(ES)	10. SPONSOR/MONITOR'S ACRONYM(S)
	11. SPONSOR/MONITOR'S REPORT NUMBER(S)

12. DISTRIBUTION/AVAILABILITY STATEMENT
Approved for public release; distribution unlimited

13. SUPPLEMENTARY NOTES

14. ABSTRACT
see report

15. SUBJECT TERMS

16. SECURITY CLASSIFICATION OF:			17. LIMITATION OF ABSTRACT	18. NUMBER OF PAGES	19a. NAME OF RESPONSIBLE PERSON
a. REPORT **unclassified**	b. ABSTRACT **unclassified**	c. THIS PAGE **unclassified**	**Same as Report (SAR)**	**20**	

Standard Form 298 (Rev. 8-98)
Prescribed by ANSI Std Z39-18

over time, a characteristic statistical spread of a given gravity wave's vertical wavenumber results, which is centered about m_0 and has a width dependent mainly on the horizontal velocity variance of the other waves in the spectrum.

Hines (1991a,b) further argued that this "Doppler spreading" of gravity wave m values was appreciable in the middle atmosphere. Advective interactions among oceanic gravity waves are also substantial (e.g., Holloway 1980; Desaubies and Smith 1982; Sherman and Pinkel 1991), and Munk (1981) speculated that spreading effects might explain the formation of spectral shapes $\sim M^{-3}$, which are often observed at large M within the ocean (e.g., D'Asaro and Morehead 1991). Since then, a number of sophisticated modeling approaches have been developed to study nonlinear interactions among oceanic gravity waves (see the review of Müller et al. 1986). Some of these models, which have sought to incorporate the major advective interactions among the waves, have generated oceanic wave spectra in agreement with observations (e.g., Orlanski and Cerasoli 1981; Flatté et al. 1985; Shen and Holloway 1986; Allen and Joseph 1989; Hibiya et al. 1996).

Hines (1991a) proposed that Doppler-spreading effects could also explain the formation of M^{-3} spectra within the atmosphere. Rather than attempting to adapt the complex models of oceanic wave dynamics to the atmosphere, Hines (1991b, 1993b) pursued an atmospheric theory by first developing a statistical model of Doppler-spread interactions among atmospheric gravity waves. This Doppler-spreading model was then combined with models of incident (unspread) wave-field spectra to derive Doppler spread fluctuation spectra (Hines 1991b, 1993b).

These Doppler-spread spectra contained features that resembled observations. For example, the theory predicted a "cutoff wavenumber" M_C, which roughly marked a transition from essentially unspread spectra at $M \ll M_C$ to Doppler spread tail spectra at $M \gg M_C$ that attenuated with increasing M. Predicted values of M_C agreed well with the locations of shape transitions in observed spectra from various regions of the atmosphere (Hines 1991b). This cutoff wavenumber assumed primary importance in a subsequent Doppler-spread parameterization of gravity-wave momentum deposition (Hines 1997a,b), which, despite including a number of untested assumptions and uncertain parameter values, performed well when used in global middle atmosphere models (Mengel et al. 1995; Lawrence 1997; Manzini et al. 1997).

Despite these successes, Doppler-spread theory could not self-consistently yield the required M^{-3} spectral shape at large M. This shortcoming was investigated in some depth by Hines (1993b). He identified the following three key approximations within the theory that could cause disagreement among predicted and observed spectra.

- *Approximation 1.* In quantifying how the velocity oscillations of all other waves affect any given gravity wave, these velocities were simplified to be
  (a) purely horizontal
  (b) invariant with time
  (c) invariant with horizontal displacement.
- *Approximation 2.* Doppler spreading was modeled using WKB wave formulas for single linear plane waves.
- *Approximation 3.* Gravity waves experienced negligible damping up to some maximum wavenumber m_M beyond which waves were completely dissipated into turbulence.

Hines (1993b) considered Approximation 1 to be the most potentially serious and, citing the oceanic model of Allen and Joseph (1989), argued that eliminating it should lead to M^{-3} Doppler-spread spectra at $M \gg M_C$. Here, we investigate this by progressively relaxing (and ultimately eliminating) Approximation 1. Our formulation attempts to maintain and build upon the analytical and illustrative approach to the Doppler-spreading problem initiated by Hines. To this end, three simple models are considered initially. They are depicted schematically in Figs. 1a–c and are addressed theoretically in sections 2–4. More detailed simulations of wave spreading follow in later sections.

2. Refraction by a stationary background wind $U(z)$

We begin by reconsidering the standard problem of a linear, small amplitude, plane gravity wave, with initial parameters m_0 (vertical wavenumber), ω_0 (intrinsic frequency), and K_0 (horizontal wavenumber), which propagates upward through a larger-scale height-varying background zonal velocity field $U(z)$, as depicted schematically in Fig. 1a. We refer to this wave hereafter as the short wave, for reasons that become clearer in section 3. For simplicity, we assume that the background Brunt–Väisälä frequency N, Coriolis parameter f, and density scale height H_ρ are constants.

Since $\partial U/\partial t = U_t = 0$, then Ω, the frequency of the short wave as measured from the ground, remains constant (e.g., Jones 1969). Since $U_x = U_y = 0$ and f is assumed to be constant, then the short wave's horizontal wavenumber K remains constant so that $K = (k^2 + l^2)^{1/2} = K_0$ (e.g., Eckermann 1992). Thus the ground-based horizontal phase speed $c_x = \Omega/K$ also remains constant. The short-wave velocity perturbation is plotted in Fig. 1a oscillating about its constant c_x value.

The intrinsic frequency of the short wave at any height z is given by the conventional Doppler relation
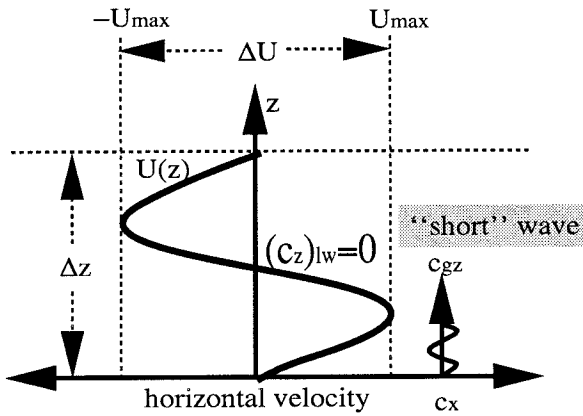
$$\omega(z) = \Omega - KU(z) \cos\varphi, \qquad (1)$$

where φ is the azimuth subtended by $\mathbf{K} = (k, l) = K(\cos\varphi, \sin\varphi)$. On propagating from height z_0 to z_1, ω varies as

a) Stationary Background Wind Profile
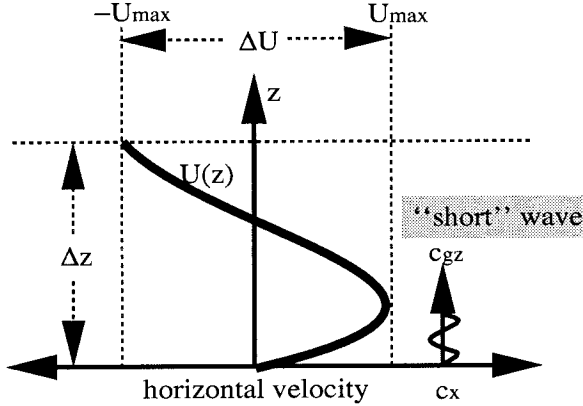
b) Stationary "Long" Wave Oscillation
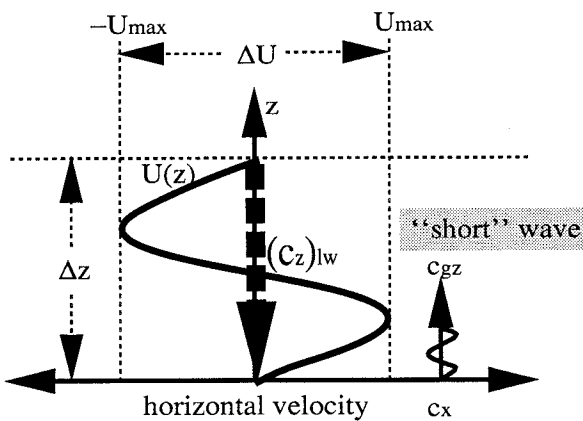

c) Propagating "Long" Wave Oscillation

FIG. 1. Schematic vertical profiles showing a "short" gravity wave of horizontal phase speed c_x and vertical group velocity c_{gz} propagating upward through (a) a background horizontal velocity profile $U(z)$; (b) a "long" wave velocity oscillation, which remains vertically stationary and has a vertical wavelength of Δz; and (c) a "long" wave, as in (b), but which propagates with a vertical phase velocity $(c_z)_{lw}$. In all three cases, the wind varies within the limits $-U_{max} \leq U(z) \leq U_{max}$ over the height interval Δz.

$$\omega(z_1) = \omega(z_0) - K[U(z_1) - U(z_0)] \cos\varphi,$$

$$= \omega(z_0) - K\Delta U \cos\varphi. \qquad (2a)$$

For simplicity, we confine wave propagation hereafter to the x–z plane so that $\varphi = 0°$ or $180°$ and $\cos\varphi = \pm 1$, whereupon (2a) simplifies to

$$\omega(z_1) = \omega(z_0) - k\Delta U, \qquad (2b)$$

where $k = K \cos\varphi = \pm K_0$.

The vertical wavenumber $m(z)$ responds to the shifts in $\omega(z)$ through the dispersion relation

$$m^2(z) = \frac{k^2[N^2 - \omega^2(z)]}{\omega^2(z) - f^2} - \alpha^2, \qquad (3a)$$

where $\alpha^2 = 1/(4H_\rho^2)$, and acoustic and forcing terms have been omitted (e.g., Marks and Eckermann 1995).

To aid a more general analysis in section 3, it proves convenient to nondimensionalize wave variables at this point. We define dimensionless frequencies $\hat{N} = N/|f|$ and $\hat{\omega} = \omega/|f|$ (so that $1 < \hat{\omega}^2 < \hat{N}^2$) and dimensionless wavenumbers, $\mu(z) = m/m_c$ and $\kappa = k/m_c$. Here m_c is an arbitrary constant wavenumber, which we use to nondimensionalize the problem: it assumes greater significance when these formulas are applied in section 3 to the Doppler-spreading problem, where it corresponds approximately to the cutoff wavenumber derived by Hines (1991b). Thus, (3a) now becomes

$$\mu^2(z) = \frac{\kappa^2[\hat{N}^2 - \hat{\omega}^2(z)]}{\hat{\omega}^2(z) - 1} - \hat{\alpha}^2, \qquad (3b)$$

where $\hat{\alpha} = \alpha/m_c$.

Since k is constant, the refraction of wave parameters is completely specified by the frequency variations given by (2) and the ensuing m variations implied by (3). Thus refraction effects are conveniently summarized by simultaneously plotting variations of the normalized variables $(\mu, \hat{\omega})$, an approach we adopt throughout this paper.

Figure 2 plots a $(|\mu|, |\hat{\omega}|)$ space using $m_c = 2\pi$ (2.5 km)$^{-1}$, $\hat{N} = 203$, and f evaluated at 45°N. Logarithmic axis scales are chosen for $|\mu|$ and $|\hat{\omega}|$ since gravity wave energy spectra are usually plotted in this fashion. The dotted curves in Fig. 2 interconnect the various $(|\mu|, |\hat{\omega}|)$ pairings that satisfy the dispersion relation (3b) for a given (constant) horizontal wavenumber κ. Hence, hereafter we refer to these dotted curves synonymously as either dispersion curves or κ curves. The $|\kappa|$ values are labeled on selected curves in Fig. 2. Note that these dispersion curves tend to flatten at $|\mu| \lesssim 0.04$ and also at the frequency limits $\hat{\omega}^2 \to \hat{N}^2$ and $\hat{\omega}^2 \to 1$. Elsewhere the curves appear linear, which indicates that the midfrequency approximation $1 \ll \hat{\omega}^2 \ll \hat{N}^2$ is accurate and (3b) can be simplified to

$$|\mu| \approx \left| \frac{\kappa\hat{N}}{\hat{\omega}} \right|. \qquad (4)$$
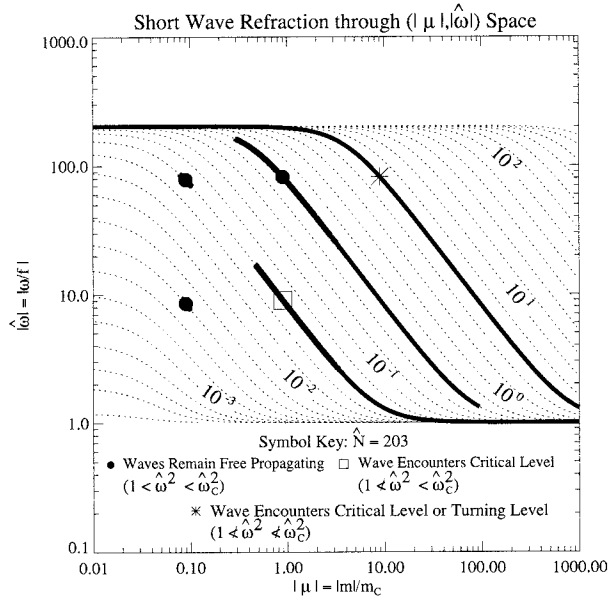
Combining (2b) and (4) then yields

FIG. 2. Dotted curves show the locus of $(|\mu|, |\hat{\omega}|)$ values satisfying the dispersion relation (3b) for a given value of $|\kappa|$. Values of $|\kappa|$ are labeled on selected curves. On moving to the right, successive curves increase in $|\kappa|$ value by a factor of $10^{0.2}$. Five waves are depicted with symbols at their initial (unrefracted) parameter values $(|\mu_0|, |\hat{\omega}_0|)$, and the solid curves show the variations of these parameters as background velocities $U(z)$ varied within the range ± 8.3 m s^{-1} ($-1 \leq \beta \leq 1$). Values of $m_c = 2\pi (2.5 \text{ km})^{-1}$ and $\hat{N} = 203$ were used at a latitude of 45°N.

$$\mu^{-1}(z_1) = \mu^{-1}(z_0) - \frac{\Delta U m_c}{N} = \mu^{-1}(z_0) - \beta, \quad (5)$$

where β encapsulates both the sense and magnitude of the short wave's refraction. This same β term arises in spectral studies of shifting of gravity wave parameters by a steady background wind (e.g., Fritts and VanZandt 1987; Gardner et al. 1993; Fritts and Lu 1993; Eckermann 1995). Substituting β back into (2b) yields

$$\hat{\omega}(z_1) = \hat{\omega}(z_0) - \kappa \hat{N} \beta. \quad (6)$$

Note from (5) that, in the midfrequency range, the amount of refraction β can be quantified solely through the change in the wave's vertical wavenumber μ, an approach used to quantify refraction effects in some previous spectral studies (Hines 1991b, 1993b; Fritts and Lu 1993). This does not, however, diminish the importance of the accompanying changes in $\hat{\omega}$, given by (6). We shall focus on this aspect of the problem in more depth later.

To illustrate these refraction effects, we consider five different short waves, each launched separately from a starting height z_0 and represented in Fig. 2 by a symbol at their initial ($\Delta U = 0$) parameter values $(|\mu_0|, |\hat{\omega}_0|)$. Each wave propagated into an environment where the background wind varied within the range $-U_{\max} \leq U(z) \leq U_{\max}$ over a height interval, Δz, as depicted in Fig. 1a. We choose $U(z_0) = 0$ and $U_{\max} = 8.3$ m s^{-1}, so that

$\beta_{\max} = U_{\max} m_c / N = 1$. Solid curves in Fig. 2 show the variations in $|\mu|$ and $|\hat{\omega}|$ that resulted for each wave.

We see in all cases that the $(|\mu|, |\hat{\omega}|)$ variations follow the relevant dispersion curve, but that those waves with larger $|\mu_0|$ values experience greater excursions through $(|\mu|, |\hat{\omega}|)$ space. Indeed, the wave represented with a square symbol in Fig. 2 is refracted to a Jones critical level [$\hat{\omega}^2 = 1$: Jones (1967)], and so is removed during propagation through this wind profile (assuming critical-level absorption). The wave depicted with an asterisk is refracted to a critical level wherever $U(z) \gtrsim 1$ m s^{-1}. At heights where $U(z) \lesssim -1$ m s^{-1}, this same wave is also refracted to a turning (reflection) level $|\hat{\omega}| \geq \hat{\omega}_c$, where $\hat{\omega}_c$ is the high-frequency cutoff [$\hat{\omega}_c \approx \hat{N}$ for $|\mu| \gtrsim 0.04$: see Marks and Eckermann (1995)]. Whether a critical level or turning level occurs first depends on the shear profile $U_z(z)$, but either way this wave does not emerge at $z = z_0 + \Delta z$ when background wind variations of this magnitude are present.

3. Doppler spreading

We now ascribe the velocity variations $-U_{\max} \leq U(z) \leq U_{\max}$ to one full vertical cycle of a "long" (small $|m|$) gravity wave oscillation of peak horizontal-velocity amplitude $U_{\max}$ and negligible vertical-velocity amplitude. This situation is depicted in Fig. 1b. Since the formulas in section 2 assumed $U_t = U_x = U_y = 0$, this interpretation assumes that the velocity structure of the long wave acts like a stationary background flow velocity $U(z)$ in refracting any given short wave that propagates through it, and thus follows Approximations 1 and 2 from section 1 (Hines 1993b).

We denote the normalized parameters of the long wave by μ_{lw}, κ_{lw}, and $\hat{\omega}_{lw}$. Our assumptions $U_t = U_x = U_y = 0$ imply that the long wave's velocity oscillation can be approximated by

$$U(z) = U_{lw}(z) = U_{\max} \sin(m_{lw}z + \vartheta_{lw}), \quad (7)$$

where $m_{lw} = m_c \mu_{lw}$ and ϑ_{lw} is the phase at $z = 0$ (taken to be zero here; see Fig 1b). We also stipulate that $\mu_{lw}^2 \gg \hat{\alpha}^2$ so that wave velocity variances do not change appreciably over one vertical wavelength due to density reductions with height.

The resulting refraction of short-wave parameters (m, ω) induced by the velocity structure (7) of the long wave is a two-wave deterministic analog of the statistical Doppler spreading among a random spectrum of gravity waves modeled by Hines (1991b, 1993b). Since the governing formulas do not differ from those presented in section 2, the solid curves in Fig. 2 can be reinterpreted here as specifying the (deterministic) Doppler spreading of these five short waves by one cycle of the long-wave oscillation in Fig. 1b.

To study this Doppler spreading of short waves in more detail, Fig. 3 extends Fig. 2 by summarizing results for a large number of short waves spanning a wide range of initial pairings $(|\mu_0|, |\hat{\omega}_0|)$. As in Fig. 2, $U_{\max} = 8.3$
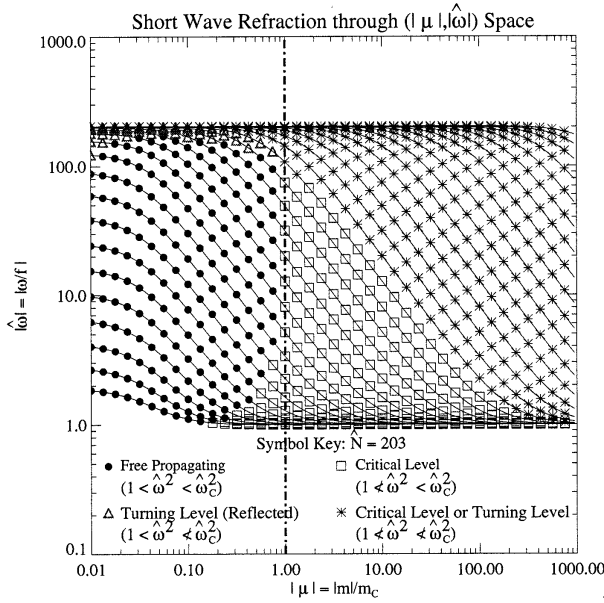
FIG. 3. As in Fig. 2 but in this case only symbols are shown at the $(|\mu_0|, |\hat{\omega}|)$ point for the waves. These symbols summarize the end result of imposing refraction within the range $-1 \leq \beta \leq 1$. Solid circles denote free propagating waves, triangles depict waves that encounter turning levels, squares denote waves that reach critical levels, and asterisks denote waves that can encounter either critical or turning levels. No free propagating waves exist at $|\mu_0| > 1$: the line $|\mu_0| = 1$ is shown with a broken curve for reference.

m s^{-1}, so that $-1 \leq \beta \leq 1$, and the symbol plotted at each $(|\mu_0|, |\hat{\omega}_0|)$ point denotes the fate of the short wave. Waves represented by filled circles propagate through the interval Δz, while the other symbols denote waves that cannot. The triangular symbols clustered near the top left of Fig. 3 indicate waves that are refracted to turning levels ($\hat{\omega}^2 = \hat{\omega}_c^2$), while square symbols show waves that are refracted to critical levels ($\hat{\omega}^2 = 1$). Asterisks identify waves that can be refracted either to a critical level or to a turning level, depending on the long-wave shear profile.

a. Cutoff vertical wavenumber m_c

Note that all short waves for which $|\mu_0| \geq 1$ ($|m| \geq m_c$) are refracted to critical levels by the long wave (a dot-dashed line at $|\mu| = 1$ is plotted in Fig. 3 for reference). Given that $\beta_{max} = 1$, this follows directly from (5). This is a simplified replication of a more general statistical result derived by Hines (1991a,b; 1993b), who predicted a cutoff in unshifted wavenumbers at $|\mu_0| \sim 1$ when $\beta_{max} \sim 1$ due to the high probability of Doppler spreading of $|\mu_0| > 1$ waves beyond a dissipative high-wavenumber limit $\mu_M = m_M/m_c$. Hines also proposed that waves at $|\mu| > \mu_M$ were obliterated (approximation 3), which, he argued, acted to relax any interacting wave spectrum for which $\beta_{max} > 1$ to an equilibrium value of $\beta_{max} \sim 1$. This in turn produced a Doppler-spread

vertical wavenumber spectrum that peaked at $|m| \approx m_c$ ($|\mu| \sim 1$) (Hines 1991b).

b. Cutoff horizontal wavenumber $k_c \approx m_c/2$

Figure 3 also reveals a cutoff horizontal wavenumber, κ_c, beyond which all waves are either absorbed at critical levels or vertically reflected at turning levels. This can be seen by starting at the bottom left of Fig. 3 and moving upward toward the $|\mu| = 1$ line, so that successively encountered dispersion curves increase in their $|\kappa|$ value. Eventually a κ curve is encountered on which there are no filled circles (i.e., no waves which propagate freely through the interval Δz). Closer inspection reveals that this occurs at $|\kappa| = \kappa_c \approx 0.5$.

This feature of the solutions is easily explained by noting that, according to (6) and the dispersion relation (3b), freely propagating short waves ($0 < |\mu| < \infty$) must satisfy the inequality

$$1 < (\hat{\omega}_0 - \kappa \hat{N} \beta)^2 < \hat{N}^2, \qquad (8)$$

assuming $\hat{\omega}_c^2 \approx N^2$ for sufficiently large $|\kappa|$ (Marks and Eckermann 1995). If $\hat{N}^2 \gg 1$, as is usually the case in the middle atmosphere, then it follows from (8) that, once

$$|\kappa \hat{N} \beta_{max}| \approx \hat{N}/2, \qquad (9)$$

no choice of $\hat{\omega}_0$ in (8) can prevent refraction of this wave either to a critical level or to a turning level as the velocity oscillation of the long wave varies β over the range $-\beta_{max} \leq \beta \leq \beta_{max}$. Since $\beta_{max} = 1$ in Fig. 3, then (9) yields no freely propagating waves at $|\kappa| \geq \kappa_c \approx 0.5$, as evident in Fig. 3. Given the Hines (1991b) arguments that Doppler-spread spectra converge to an equilibrium of $\beta_{max} \sim 1$, then our finding of $\kappa_c \approx 0.5$ for $\beta_{max} = 1$ illustrates that a cutoff horizontal wavenumber $k_c \approx m_c/2$ is also predicted by the Doppler-spread model of Hines (1991b, 1993b), as extended here.

The "case III" model of oceanic gravity waves of Allen and Joseph (1989) predicted M^{-3} and $\mathcal{K}^{-3}$ spectra beyond hypothesized Eulerian cutoff wavenumbers M_c and $\mathcal{K}_c$, respectively, where $\mathcal{K}$ is the one-dimensional horizontal Fourier wavenumber (see also Chunchuzov 1996). On quantifying M_c in the atmosphere using Doppler-spread theory (i.e., $M_c \sim m_c$), Hines (1991b, 1993b) cited their findings as evidence that a fully generalized Doppler-spread theory should yield M^{-3} spectra at $M \gg m_c$ as observed. Spectral analysis of high-resolution velocity and temperature data from stratospheric aircraft by Bacmeister et al. (1996) revealed a clear transition from shallower power-law spectra at smaller horizontal wavenumbers to $\mathcal{K}^{-3}$ spectra at large $\mathcal{K}$. This transition occurred at a wavenumber of $\sim 2\pi$ (5 km)$^{-1}$, which is of the order of $k_c = m_c/2$ at these heights (e.g., Tsuda et al. 1991; Allen and Vincent 1995). Bacmeister et al. (1996) noted that separable linear spectral models

also predict the observed spectral shapes and transition point quite well ($k_c = m_c$ in these models).

c. Approximation 1 and the "longness" criterion

Hines (1991b, 1993b) employed Approximation 1 to model Doppler spreading among waves of all wavelengths and arbitrary amplitudes, without testing this approximation in any formal way. As a necessary first condition for Approximation 1 to hold, we imposed scale separation between the long and short wave through a longness criterion $|\mu_{lw}| \ll |\mu_0|$ and thereafter assumed that the approximation was valid. Yet $|\mu_{lw}| \ll |\mu_0|$ is well satisfied when $|\kappa_{lw}| \gg |\kappa|$ and/or $|\hat{\omega}_{lw}| \gg |\hat{\omega}_0|$, whereas Approximation 1 requires the long wave to appear approximately stationary and horizontally invariant to the short wave, which requires (at least) that $|\kappa_{lw}| \ll |\kappa|$ and $|\hat{\omega}_{lw}| \ll |\hat{\omega}_0|$. Thus, a better longness criterion is $|\kappa_{lw}| \ll |\kappa|$, since this usually also ensures that both $|\mu_{lw}| \ll |\mu_0|$ and $|\hat{\omega}_{lw}| \ll |\hat{\omega}_0|$. We impose this hereafter, so that the long wave must now lie in the bottom left region of Figs. 2–3, and initial short-wave values ($|\mu_0|$, $|\hat{\omega}_0|$) must lie to the right and above this ($|\mu_{lw}|$, $|\hat{\omega}_{lw}|$) point in Figs. 2–3.

However, even in these cases Approximation 1 may not be valid. For example, in sections 2 and 3 our initial longness criterion $|\mu_{lw}| \ll |\mu_0|$ in no way justified neglecting the U_z variations of the long wave that refracted the short wave. In the same way, $|\kappa_{lw}| \ll |\kappa|$ and $|\hat{\omega}_{lw}| \ll |\hat{\omega}_0|$ do not automatically imply that U_x and U_t terms can be ignored in computing the propagation of the short wave (Approximations 1c and 1b, respectively). However, since Approximation 2 is usually assured by our longness criterion (e.g., Eckermann and Marks 1996; see also section 9), we can use WKB ray theory to trace any given short wave through a long wave without discarding the horizontal and temporal oscillations of the long wave, thereby assessing directly the validity of Approximation 1. We pursue this in the following sections.

4. Short-wave ray solutions in the presence of a propagating long wave

In tackling this problem, we consider again the idealized background atmosphere described in section 2. As in section 3, the background velocity is produced by a long wave of constant and steady amplitude. We allow this long wave to propagate upward through the atmosphere as an infinite wave train with (constant) parameters m_{lw}, ω_{lw}, and K_{lw}, which satisfy the dispersion relation (3a). We set $m_{lw} < 0$ and $\omega_{lw} > 0$ so that the vertical phase velocity is downward ($(c_z)_{lw} < 0$) and vertical group velocity is upward ($(c_{gz})_{lw} > 0$). We also confine long-wave propagation along the x axis so that $K_{lw} = k_{lw}$ and the phase of the long wave is given by

$$\theta_{lw}(x, z, t) = k_{lw}x + m_{lw}z - \omega_{lw}t + \vartheta_{lw}, \quad (10)$$

since $\Omega_{lw} = \omega_{lw}$ here.

We launch the short wave from a position (x_0, z_0), at a time t_0 when $\theta_{lw}(x_0, z_0, t_0)$ delivers a node in the long wave's velocity oscillation (see section 4b). This situation is profiled vertically in Fig. 1c, where the propagation of the long wave is depicted by arrowing its downward vertical phase velocity $(c_z)_{lw}$.

a. Wave action equation

We omit damping from this problem, following Approximation 3, so that the long wave and short wave both conserve wave action. For the short wave,

$$\frac{\partial A}{\partial t} + \nabla \cdot [(\mathbf{U} + \mathbf{c}_g)A] = 0, \quad (11)$$

where $A = E/\omega$ is the short wave's action density, E is its total energy density, $\mathbf{U}$ is the background velocity, and $\mathbf{c}_g = (c_{gx}, c_{gy}, c_{gz})$ is the intrinsic group velocity of the short wave (Andrews and McIntyre 1978).

b. Velocity oscillation of the long wave

A wave action solution for the long wave that remains valid in a vertically varying background velocity field is

$$(B_z)_{lw} = (c_{gz})_{lw}A_{lw} = \text{const}, \quad (12)$$

where $(B_z)_{lw}$ is the vertical flux of long-wave action density (e.g., Schoeberl 1985). As in section 3, we assume $\mu_{lw}^2 \gg \hat{\alpha}^2$, whereupon the background density ρ is approximately constant across the interval Δz in Fig. 1c. This in turn yields, through (12), an approximately constant peak horizontal velocity amplitude U_{max}, and a long-wave velocity oscillation, $\mathbf{U}_{lw}(x, z, t) = (U_{lw}(x, z, t), V_{lw}(x, z, t), W_{lw}(x, z, t))$, given by

$$U_{lw}(x, z, t) = U_{max} \sin\theta_{lw}(x, z, t) \quad (13a)$$

$$V_{lw}(x, z, t) = \left(\frac{-f}{\omega_{lw}}\right) U_{max} \cos\theta_{lw}(x, z, t) \quad (13b)$$

$$W_{lw}(x, z, t) = \left(\frac{-k_{lw}}{m_{lw}}\right) U_{max} \sin\theta_{lw}(x, z, t) \quad (13c)$$

(e.g., Gossard and Hooke 1975). We ignore influences of the temperature and density perturbations of the long wave on the propagation of the short wave since they are usually minor (e.g., Henyey and Pomphrey 1983; Zhong et al. 1995; Eckermann and Marks 1996).

The velocity oscillation of the long wave along the x–z plane is depicted in Fig. 4, extending the simple one-dimensional depiction of the problem in Fig. 1c. The phase fronts of the long wave lie along the x' axis and move downward with time along the z' axis at the phase speed $C_{lw} = -|\mathbf{c}_{lw}|$, where $\mathbf{c}_{lw}$ is the phase velocity.
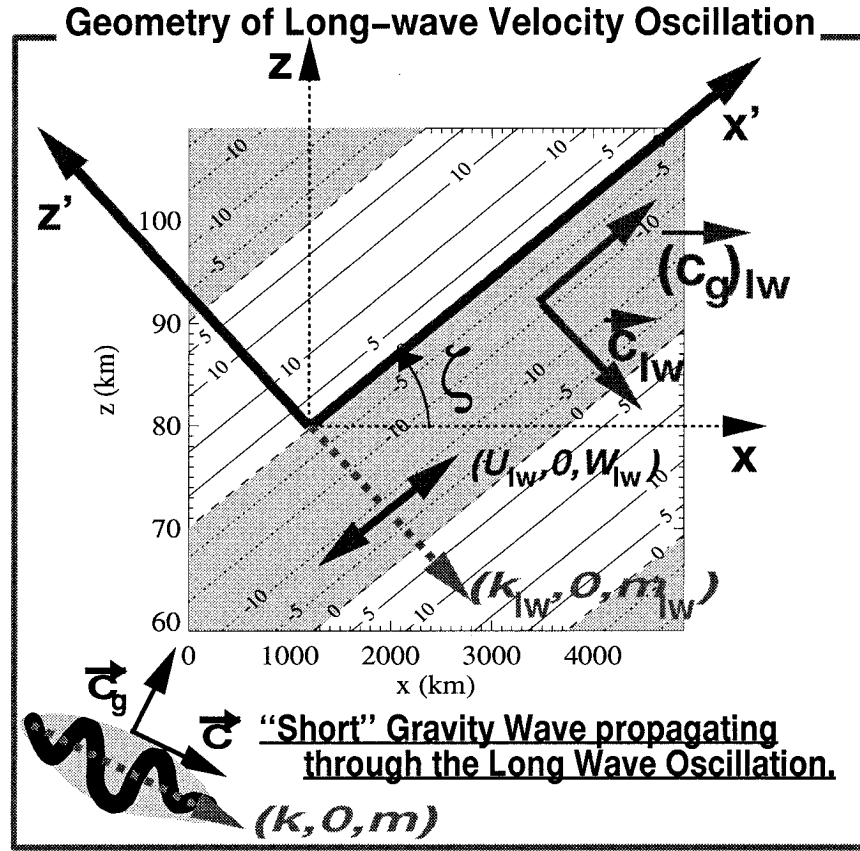
FIG. 4. Contour plot of a sample long-wave velocity oscillation (with contour labels in m s^{-1} and phases of negative velocities shaded). This wave has a peak velocity amplitude of 11 m s^{-1}. Various vectors on the plot show the long wave's wavenumber $(k_{\mathrm{lw}}, 0, m_{\mathrm{lw}})$, its velocity perturbation along the x–z plane, $(U_{\mathrm{lw}}, 0, W_{\mathrm{lw}})$, its group velocity $(\mathbf{c}_g)_{\mathrm{lw}}$, and its phase velocity $\mathbf{c}_{\mathrm{lw}}$. The rotated axes (x', z') are explained in the text. A short gravity wave of wavenumber $(k, 0, m)$ is depicted at the bottom left impinging upon this long wave.

c. Ray equations for the short wave

The short wave is depicted in the bottom left of Fig. 4, and we use ray equations to compute its propagation through the long wave. Its wavenumber components are governed by the refraction equations (e.g., Jones 1969)

$$\frac{dk}{dt} = -k\frac{\partial U_{\mathrm{lw}}}{\partial x} - m\frac{\partial W_{\mathrm{lw}}}{\partial x} \qquad (14a)$$

$$\frac{dm}{dt} = -k\frac{\partial U_{\mathrm{lw}}}{\partial z} - m\frac{\partial W_{\mathrm{lw}}}{\partial z}, \qquad (14b)$$

where d/dt is time differentiation following the group motion of the short wave. The wavenumber vector (k, l, m) is again taken to be zonally aligned $(l = 0)$ and remains so since $\partial \mathbf{U}_{\mathrm{lw}}/\partial y = 0$ and, thus, $dl/dt = 0$. The time variation of the long-wave background yields an additional short-wave ray equation (e.g., Jones 1969; Eckermann and Marks 1996)

$$\frac{d\Omega}{dt} = k\frac{\partial U_{\mathrm{lw}}}{\partial t} + m\frac{\partial W_{\mathrm{lw}}}{\partial t}, \qquad (15)$$

where Ω is the ground-based frequency of the short wave.

d. Transformation to the "long-wave frame"

Solutions of the short-wave ray equations in this case follow on reformulating the problem within a reference frame that moves with the phase of the long wave. First, we transform to the rotated coordinate axes (x', z') in Fig. 4, where

$$\begin{pmatrix} x' \\ z' \end{pmatrix} = \begin{pmatrix} \cos\zeta & -\sin\zeta \\ \sin\zeta & \cos\zeta \end{pmatrix}\begin{pmatrix} x \\ z \end{pmatrix}, \qquad (16)$$

and $\zeta = \arctan(-k_{\mathrm{lw}}/m_{\mathrm{lw}})$ is the elevation of the long wave's phase fronts above the horizontal plane. Since there are no long-wave phase variations along x', then, when viewed from this frame, the phase (10) transforms to

$$\theta'_{\mathrm{lw}}(z', t) = m'_{\mathrm{lw}}z' - \omega t = -K_{\mathrm{lw}}^{\mathrm{tot}}z' - \omega t, \qquad (17a)$$

where m'_{lw} is the wavenumber component along z', which equals the total wavenumber $K_{\mathrm{lw}}^{\mathrm{tot}} = (k_{\mathrm{lw}}^2 +$

$m_{lw}^2)^{1/2}$ in magnitude but is negative ($m'_{lw} = -K_{lw}^{tot}$) since the long-wave phase moves downward along z' at the phase velocity $C_{lw} = -\omega_{lw}/K_{lw}^{tot} = \omega_{lw}/m'_{lw}$. Thus (17a) can be reexpressed as

$$\theta'_{lw}(z', t) = m'_{lw}(z' - C_{lw}t). \qquad (17b)$$

Given a general Galilean transformation to another similarly tilted nonaccelerated reference frame

$$(x'', y'', z'') = (x', y', z') - \mathbf{V}t, \qquad (18)$$

then choosing $\mathbf{V} = (0, 0, C_{lw})$ in (18) transforms to a new frame (x'', z'') that has the same orientation as (x', z') in Fig. 4 but moves downward along z' at the long-wave phase velocity C_{lw}.

We refer to (x'', z'') for $\mathbf{V} = (0, 0, C_{lw})$ as the long-wave frame since it is oriented with the phase fronts of the long wave and follows their movement. Since $z'' = z' - C_{lw}t$, then from (17b) the long-wave phase is given by

$$\theta''_{lw}(z'') = m'_{lw}z'' = -K_{lw}^{tot}z'', \qquad (19)$$

and so the velocity oscillation of the long wave remains stationary within this long-wave frame. Due to the transverse nature of the long-wave oscillation along the x–z plane, its phase varies only along z'', while its velocity oscillates along the x'' ($=x'$) axis (see Fig. 4), and thus (13a) and (13c) transform and then combine to yield

$$U''_{lw}(z'') = \mathcal{U}_{max} \sin\theta''_{lw}(z''), \qquad (20)$$

where $U''_{lw}(z'')$ is the velocity along the x'' axis, and $\mathcal{U}_{max}$ is the peak *total* velocity amplitude of the long wave in the x–z plane and equals $U_{max}[1 + (k_{lw}/m_{lw})^2]^{1/2} = U_{max}|\sec\zeta|$. The remaining velocity component (13b), which does not influence short-wave propagation, oscillates orthogonal to the page in Fig. 4, producing elliptical orbits in the x–y plane.

e. Ray solutions for the short wave

Next we transform the ray and action equations for the short wave to the long-wave frame (x'', z''). Since A is invariant under Galilean transformations (e.g., Grimshaw 1984), then, using (20), the continuity equation for action density (11) takes the form

$$\frac{\partial A}{\partial t} + \frac{\partial}{\partial x''}([U''_{lw} + c''_{gx''}]A) + \frac{\partial}{\partial z''}(c''_{gz''}A) = 0 \quad (21)$$

in the long-wave frame, where $c''_{gx''}$ and $c''_{gz''}$ are components of the short wave's group velocity along x'' and z'', respectively. Since the long wave produces gradients along z'' alone, according to (19) and (20), then the first two terms in (21) vanish, giving the solution (Thorpe 1989; Eckermann and Marks 1996)

$$B''_{z''} = c''_{gz''}A$$

$$= \{(c_{gz}\cos\zeta - c_{gx}\sin\zeta) - C_{lw}\}A = \text{const.} \quad (22)$$

Thus the flux of short-wave action density along z'', $B''_{z''}$, is conserved.

In the long-wave frame the ray equations (14)–(15) become

$$\frac{dk''}{dt} = -k''\frac{\partial U''_{lw}}{\partial x''} = 0 \qquad (23a)$$

$$\frac{dm''}{dt} = -k''\frac{\partial U''_{lw}}{\partial z''} \qquad (23b)$$

$$\frac{d\Omega''}{dt} = k''\frac{\partial U''_{lw}}{\partial t} = 0, \qquad (23c)$$

where k'' and m'' are the wavenumber components of the short wave along x'' and z'' respectively, which relate to those along x and z according to

$$\begin{pmatrix} k'' \\ m'' \end{pmatrix} = \begin{pmatrix} \cos\zeta & \sin\zeta \\ -\sin\zeta & \cos\zeta \end{pmatrix}\begin{pmatrix} k \\ m \end{pmatrix}, \qquad (24)$$

and Ω'' is the short-wave frequency in the long-wave frame, which relates to Ω through the standard Doppler relation

$$\Omega'' = \Omega - C_{lw}m''. \qquad (25)$$

Equations (23a) and (23c) vanish according to (20) so that k'' and Ω'' are both constants during propagation through the long wave. The remaining ray equation (23b) is redundant since m'' follows from the dispersion relation (3), so that

$$\omega^2 = (\Omega'' + C_{lw}m'' - k''U''_{lw})^2$$

$$= \frac{k^2N^2 + (m^2 + \alpha^2)f^2}{k^2 + m^2 + \alpha^2}. \qquad (26)$$

f. Simplifications for $|k_{lw}| \ll |m_{lw}|$ ($\zeta \to 0$) as a test of Approximation 1b

Our amended longness criterion of section 3c was $|k_{lw}| \ll |k|$, so that $|\omega_{lw}| \ll |\omega|$ and $|m_{lw}| \ll |m|$. The implied low frequency of the long wave also implies $(k_{lw}/m_{lw})^2 = \tan^2\zeta \ll 1$ through the dispersion relation (3a), and thus $\zeta \approx 0$.

Thus, to simplify our analysis of these short-wave solutions, we consider first the inertial limit $\zeta = 0$, which eliminates horizontal variations of the long-wave oscillation ($k_{lw} \to 0$) but retains its temporal oscillation. The velocity oscillations of the long wave now become purely horizontal, and the long-wave phase moves downward along z at the vertical phase velocity $(c_z)_{lw}$, consistent with the simplified depiction in Fig. 1c. This invokes approximations 1a and 1c but not approximation 1b, and thus allows us to isolate and test approximation 1b.

The short-wave solutions now simplify to those derived by Broutman and Young (1986). The wave action solution (22) becomes

$$[c_{gz} - (c_z)_{lw}]A = \text{const.} \qquad (27)$$

The horizontal wavenumber k is constant, and

$$\Omega'' = \Omega - (c_z)_{\mathrm{lw}}m = \mathrm{const}, \qquad (28)$$

while m is determined by the dispersion relation

$$\omega^2 = (\Omega'' + (c_z)_{\mathrm{lw}}m - kU_{\mathrm{lw}})^2$$

$$= \frac{k^2N^2 + (m^2 + \alpha^2)f^2}{k^2 + m^2 + \alpha^2}. \qquad (29)$$

Solving (29) for m yields a quartic polynomial with two real and two imaginary roots for free-propagating waves, and the relevant real root for m is easily identified. The general form of these solutions for m can be

illustrated by adopting the midfrequency approximation (4) so that (29) simplifies to

$$\omega(z, t) = \Omega'' + (c_z)_{\mathrm{lw}}m(z, t) - kU_{\mathrm{lw}}(z, t)$$

$$= -\frac{kN}{m(z, t)}. \qquad (30)$$

The minus sign on the right-hand side of (30) is inserted to ensure downward vertical phase propagation for negative m and positive ω. Solving for m in (30) yields a quadratic with roots (Broutman and Young 1986).

$$m(z, t) = \frac{-[\Omega'' - kU_{\mathrm{lw}}(z, t)] \pm \{[\Omega'' - kU_{\mathrm{lw}}(z, t)]^2 - 4kN(c_z)_{\mathrm{lw}}\}^{1/2}}{2(c_z)_{\mathrm{lw}}}. \qquad (31)$$

Since $(c_z)_{\mathrm{lw}} < 0$, the discriminant in (31) is always positive, so solutions always exist. This is not always so in the full quartic solution, where solutions are imaginary when the wave is refracted to a turning level ($\omega^2 > \omega_c^2$). The negative $(c_z)_{\mathrm{lw}}$ also ensures one positive and one negative root for m in (31), and we choose the latter since we set $m < 0$ initially.

5. Limiting behavior of the $\zeta = 0$ short-wave solutions

We now consider two asymptotic limits of the simplified ($\zeta = 0$) short-wave solutions of section 4f. In defining these limits, it proves useful to introduce the ratio

$$r = \frac{-c_{gz}}{(c_z)_{\mathrm{lw}}}, \qquad (32)$$

which we call the phase–group ratio. The wave action solution (27) can now be reexpressed as

$$-(c_z)_{\mathrm{lw}}A(r + 1) = c_{gz}A(1 + r^{-1})$$

$$= B_z(1 + r^{-1}) = \mathrm{const}, \qquad (33)$$

where $B_z = Ac_{gz}$ is the vertical flux of short-wave action density.

a. The "fast" limit: $r \gg 1$, $r \to \infty$

For $r \gg 1$, then $c_{gz} \gg -(c_z)_{\mathrm{lw}}$ and so the short-wave packet propagates upward much faster than the downward moving long-wave phase fronts. Thus, the time that the short wave takes to propagate through one vertical wavelength of the long wave is very much less than the period of the long wave.

"Fast limit" solutions follow by letting $r \to \infty$, whereupon the solutions of section 4f reduce to those of section 3. Equation (33) simplifies to the familiar conser-

vation with height of $B_z = c_{gz}A$ (e.g., Schoeberl 1985), the same solution that governs the amplitude of the long wave in section 4b and of waves in Doppler-spread theory (Hines 1991b). Similarly, $(c_z)_{\mathrm{lw}}m$ becomes negligibly small in this limit, whereupon (28) and (29) reduce to the original equations (1) and (3a) that we used in section 3 to model spreading effects initially.

Thus the longness criterion of section 3c is a necessary but insufficient condition for Approximation 1b to hold. We see here that r must also remain sufficiently larger than unity in order for the short-wave solutions of section 4f to be approximated acceptably by the $r \to \infty$ solutions of Approximation 1.

b. The "slow" limit: $0 < r \ll 1$, $r \to 0$

For $c_{gz} \ll -(c_z)_{\mathrm{lw}}$ and thus $0 < r \ll 1$, the vertical group propagation of the short wave is much slower than the speed of the long-wave phase fronts. Thus, the vertical distance travelled by the short wave during one period of the long wave is very much less than the vertical wavelength of the long wave. This is easily seen from Fig. 1c: the long wave propagates its phase rapidly through the short wave for $c_{gz} \ll -(c_z)_{\mathrm{lw}}$, so that many long-wave cycles pass through the short wave as it propagates slowly upward through the interval Δz.

In the slow limit $r \to 0$, the ray equations (14a) and (14b) vanish so that m, k, and hence ω remain constant for the short wave, as originally discussed by Jones (1969) (see also Zhong et al. 1995; Eckermann and Marks 1996). From (33), $(c_z)_{\mathrm{lw}}A$ remains constant; since $(c_z)_{\mathrm{lw}}$ is also constant in this problem, then

$$A = \mathrm{const}. \qquad (34)$$

Thus, if short waves were to near this slow limit, then little short-wave refraction would occur and waves would tend to conserve their action densities A (see also Broutman et al. 1997).
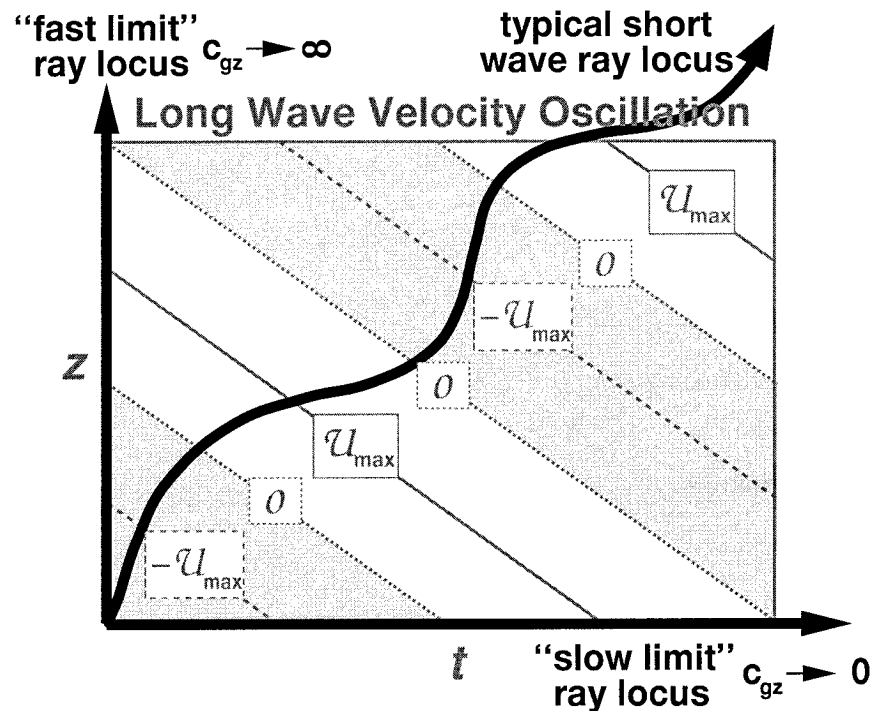
FIG. 5. Schematic contour plot of an upward propagating long-wave velocity oscillation as a function of time t and height z, with each axis spanning one long-wave cycle. The thick linear arrows show the hypothetical time–height history of a short-wave trajectory through the long wave implied by the "fast limit" and "slow limit" solutions, which short-wave solutions might approach but never attain. The curved black arrow depicts the time–height locus of a typical short-wave trajectory through the long wave (e.g., Fig 2 of Eckermann and Marks 1996).

For upward propagating waves, it can be shown that the refraction of any given short wave by a long wave always lies somewhere between (but never equals) these fast and slow limits. Of course, most short-wave solutions differ significantly from either limit, as shown in Fig. 5, since changes in m, Ω, and ω are all significant during propagation (see also Eckermann and Marks 1996). This is investigated in more depth in sections 6–8.

c. The "antipropagating" solutions: $r < 0$

When $r < 0$ and c_{gz} and $(c_z)_{lw}$ have the same sign, the long wave and short wave propagate in opposing vertical directions. In this case, the range of refraction of short-wave parameters by the long wave can exceed the fast limit described above, as discussed by Eckermann and Marks (1996).

This situation is more relevant to gravity waves in the ocean, where upward propagating and downward propagating gravity waves coexist with approximately equal energies (e.g., Munk 1981; D'Asaro and Morehead 1991). Here, the "phase–group condition" $c_{gz} = (c_z)_{lw}$ ($r = -1$) in particular has received considerable attention, initially because it was where certain resonant wave–wave interactions were thought to interchange wave action most efficiently (e.g., McComas and Bretherton 1977). The phase–group condition produces $A \rightarrow$

∞ according to (33) and is a caustic where ray theory fails (Broutman 1986). Using a midfrequency approximation, $r = -1$ occurs when $\Omega'' - kU_{lw}(z, t) \rightarrow 0$ (Broutman and Young 1986), so the mathematical condition for the singularity resembles a critical-level-type condition as viewed within the long-wave frame: indeed, the conventional critical level follows from these solutions as $(c_z)_{lw} \rightarrow 0$. However, phase–group caustics differ physically from critical levels in that m remains finite [see (31)], and short waves can survive these encounters. Accurate analysis of these events requires an extended ray theory that deals properly with the caustic singularity (e.g., Broutman 1986; Broutman et al. 1997).

Since gravity wave variance is dominated by upward propagating ($r > 0$) waves (e.g., Hirota and Niki 1985; Eckermann et al. 1995), antipropagating solutions are less immediately relevant to the atmosphere, and so we confine attention in the remainder of the paper to $r > 0$ solutions. Nevertheless, short waves undergoing successive reflections at turning levels may experience some of these antipropagating interactions with long waves during the downward portions of their group propagation. For example, the "separatrix crossings" at phase–group caustics (Broutman and Young 1986; Bruhwiler and Kaper 1995) resemble aspects of the Eckart's resonances for ducted modes considered by Fritts and
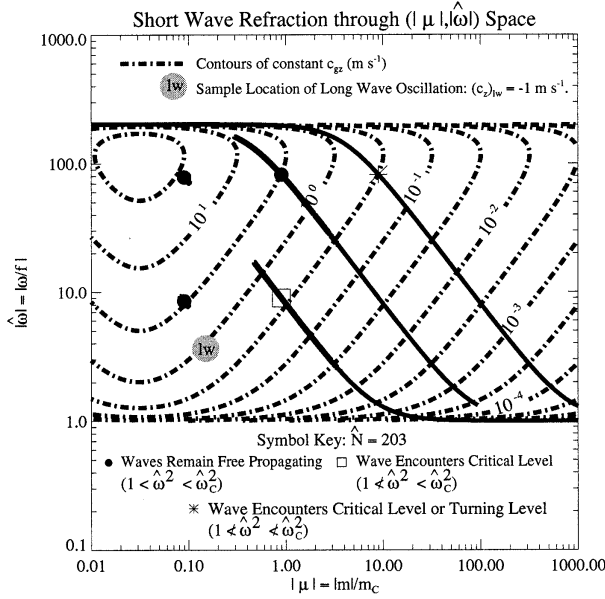
FIG. 6. A reproduction of Fig. 2, with contours of constant c_{gz} values plotted with thick broken curves and contour labels in meters per second. A sample long wave of $(c_z)_{lw} = -1$ m s^{-1} is also shown on this plot. Thus, if we assume that this long wave refracts the short waves, the contours can also be interpreted as phase/group ratios r for the short waves.
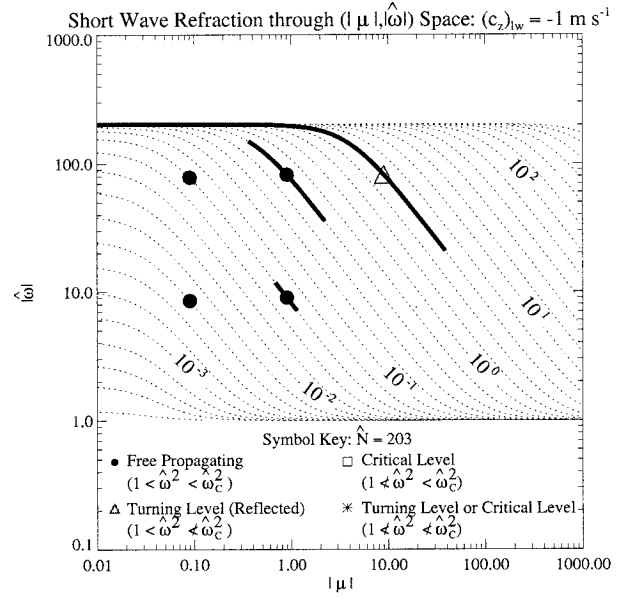

FIG. 7. As in Fig. 2 but in this case the short-wave refraction was computed using the $\zeta = 0$ short-wave solutions of section 4f assuming a long wave of $(c_z)_{lw} = -1$ m s^{-1}.

Yuan (1989). We also show in appendix A that upward propagating gravity waves may undergo similar sorts of caustic interactions in environments where the mean flow has a downward component.

d. Phase–group ratios of refracted short waves

Figure 6 reproduces the refraction of the five short waves in Fig. 2, which used the solutions of section 3. A sample long wave is depicted in Fig. 6 with a shaded circle and is positioned to the left and below the initial position of the three largest-$|\mu_0|$ short waves, thereby satisfying longness criteria for these waves initially. This long wave has a vertical phase speed $(c_z)_{lw} = -1$ m s^{-1}, and we assume that the short waves in Fig. 6 were refracted by it.

The labeled broken curves in Fig. 6 are contours of constant vertical group velocity c_{gz}. As the short waves are refracted to larger $|\mu|$ values, they intersect contours of progressively smaller c_{gz} values. Since $(c_z)_{lw} = -1$ m s^{-1}, then from (32) these contours can be interpreted here as r values for these short waves. Clearly, as short waves are refracted by the long wave to $|\mu| \gg 1$, then $0 < r \ll 1$, and so, if anything, they tend more towards the slow limit of section 5b rather than the fast limit $r \gg 1$ that was implicitly assumed when computing their refraction in section 3.

This result, together with the findings of section 5a, reveal that approximation 1b fails for the short waves at both large and intermediate $|\mu|$ values. In light of this,

we now recompute the refraction of short waves using the $\zeta = 0$ shortwave solutions of section 4f that do not use approximation 1b.

6. Shortwave refraction by a vertically propagating long wave

Figure 7 displays the five short waves previously considered in Figs. 2 and 6. Here, their refraction was computed using the ray solutions in section 4f, assuming a long-wave phase speed $(c_z)_{lw} = -1$ m s^{-1}, as in Fig. 6. Given initial short-wave parameters (m_0, ω_0) at the node of the long-wave velocity oscillation, then, from (29), ω varies as

$$\omega = \omega_0 - kU_{lw} + (m - m_0)(c_z)_{lw}, \qquad (35)$$

while m varies so as to satisfy the dispersion relation (3a).

We note immediately from Fig. 7 that the range of short-wave refraction is reduced substantially compared to Fig. 2. This is consistent with the inferences from Fig. 6, where waves at $|\mu| \gg 1$ tended toward $0 < r \ll 1$, and so their refraction characteristics should more closely resemble the slow limit solutions of section 5b, in which no variation of short-wave parameters occurs.

This suppression of short-wave refraction can also be understood on inspecting (35). As short waves are refracted to $|m| > |m_0|$, then $-kU_{lw}$ is negative (since ω must decrease) but $(m - m_0)(c_z)_{lw}$ is positive [recall that m, m_0, and $(c_z)_{lw}$ are all negative]. Thus, the feedback effect of the latter term in (35) reduces the refraction compared to (2b). Similarly, when $-kU_{lw}$ is positive and $|m| < |m_0|$ in (35), then $(m - m_0)(c_z)_{lw}$ is negative,
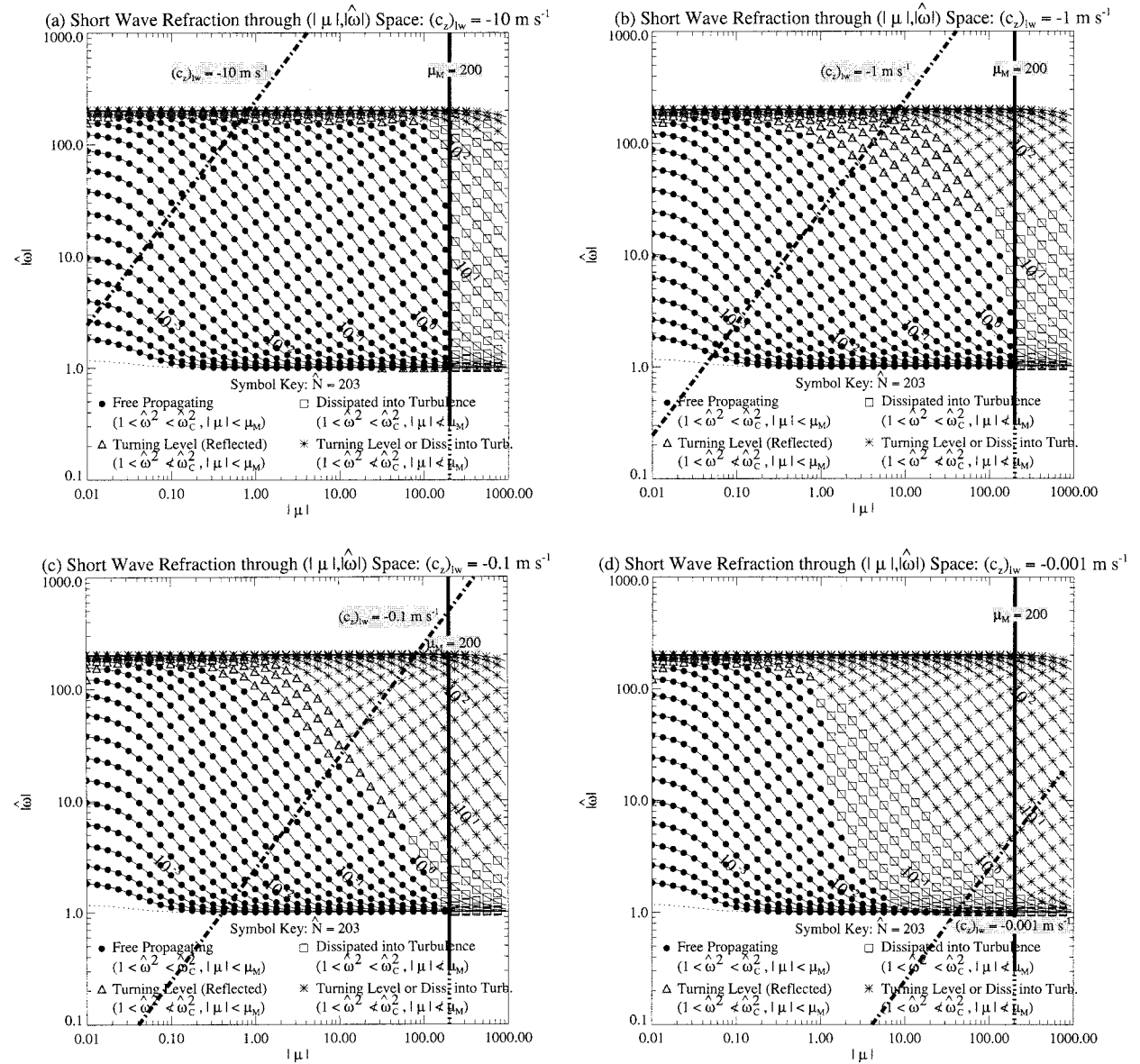
FIG. 8. As in Fig. 3 but using the $\zeta = 0$ short-wave solutions of section 4f assuming a long wave of (a) $(c_z)_{lw} = -10$ m s^{-1}, (b) $(c_z)_{lw} = -1$ m s^{-1}, (c) $(c_z)_{lw} = -0.1$ m s^{-1}, and (d) $(c_z)_{lw} = -0.001$ m s^{-1}. The $|(c_z)_{lw}|$ isoline is shown with a broken curve, and so the long wave must lie somewhere along it in each case. The critical-level criterion is replaced here with a dissipative criterion, $|\mu| \geq \mu_M = 200$.

which again reduces the refraction in (35) compared to (2b).

The feedback term $(m - m_0)(c_z)_{lw}$ also produces changes in the ground-based frequency Ω, according to (28) (since Ω'' is constant). These changes oppose the changes in ω due to the long-wave velocity U_{lw}. Note that the feedback term is limited in magnitude as $m \to 0$ and so cannot ultimately prevent turning levels. However, as $m \to \infty$, then $(m - m_0)(c_z)_{lw} \to \infty$, which from (29) ensures that critical levels do not occur: the accelerations of the long-wave oscillation always refract short waves away from a Jones critical level ($\omega = f$) (Eckermann and Marks 1996).

Thus, in repeating the presentation of Fig. 3 using these short-wave ray solutions, a critical-level criterion is no longer relevant. We replace it by following Approximation 3 of Hines (1993b) and introducing a maximum wavenumber μ_M, beyond which waves are dissipated completely into turbulence. A value of $\mu_M = 200$ is adopted from section 4 of Hines (1991b).

Figure 8 shows four plots, each depicting the end result of subjecting short waves to a long-wave velocity oscillation U_{lw} in the range ± 8.3 m s^{-1} ($\beta_{max} = 1$), for which the theory of section 3 predicted a sharp cutoff at $|\mu_0| \sim 1$. In each plot, a different value of $(c_z)_{lw}$ was used: (a) -10 m s^{-1}, (b) -1 m s^{-1} (as in Figs. 6–7),

(c) -0.1 m s^{-1}, and (d) -10^{-3} m s^{-1}. The $|(c_z)_{lw}|$ isoline is shown with a broken curve on each plot, and the long wave must lie somewhere along it in each case. The line $|\mu| = \mu_M$ is also shown.

Clearly the results in Figs. 8a–c differ substantially from those in Fig. 3. In Fig. 8a, the characteristics at $|\mu| < \mu_M$ are nearly independent of $|\mu|$, with free propagating short waves occurring everywhere except at $|\hat{\omega}_0| \gtrsim 150$. In Fig. 8b $[(c_z)_{lw} = -1$ m s$^{-1}]$, a collection of waves appear at $1 \gtrsim |\mu_0| \gtrsim 100$ that are now reflected at turning levels by the long wave. For $(c_z)_{lw} = -0.1$ m s^{-1} in Fig. 8c, we now see that waves for which $|\kappa| \gtrsim 10^{0.3}$ can no longer propagate freely. Note, however, that there is still no evidence of a short-wave cutoff at $|\mu_0| \sim 1$—many free-propagating short waves still exist at $|\mu_0| \gg 1$. Only as $(c_z)_{lw} \rightarrow 0$ do characteristics resembling those in Fig. 3 return in Fig. 8d (since $r \gg 1$). However, the $|(c_z)_{lw}|$ isoline in Fig. 8d, on which the long wave must lie, yields $|\mu_{lw}| \gg 1$, whereupon the longness criterion is violated for most short waves on this diagram.

Thus we conclude that incorporating the vertical propagation of the long wave removes any tendency for a distinct cutoff in free-propagating short waves at $|\mu_0| \sim 1$ when maximum normalized long-wave wind variations of $\beta_{max} = 1$ are present, in contrast to the findings of Doppler-spread theory. Note, however, that the Doppler-spread analysis of Hines (1991b, 1993b) did not impose any longness criteria on interacting waves, and so it could still simulate a cutoff since it would not reject the results in Fig. 8d (even though Approximations 1 and 2 mostly fail in this case).

We shall now look to incorporate additional effects that we have omitted up to this point, to see whether they affect these findings in any significant way.

7. Effect of the vertical velocity and horizontal wavelength of the long wave (Approximations 1a and 1c)

Approximation 1 also neglects the effects of long-wave vertical velocities (Approximation 1a) and horizontal wavelengths (Approximation 1c), as has our analysis up to this point. Hines (1991b, 1993b) extended his analysis to investigate how larger-scale vertical velocities might modify his Doppler-spread theory (see also appendix A). We can gauge the effects in our simplified solutions by now considering the general ($\zeta \neq 0$) ray solutions of section 4e, in which the effect of both the vertical velocity and the horizontal wavelength of the long wave on the short wave are included.

Figure 9 considers the same five short waves depicted in earlier figures. Here, these waves were refracted by a long wave with $(c_z)_{lw} = -1$ m s^{-1} and $\zeta = -1.5°$ (panel a) and $+1.5°$ (panel b). These small ζ values yield only small W_{lw} values, but $|\zeta|$ values any larger than these yield high-frequency long-wave oscillations and violations of longness criteria for the short waves.

Since $k_{lw} \neq 0$ here, (14a) no longer vanishes, so some spreading of short-wave k values now occurs. Thus, the refraction of short waves in Fig. 9 is no longer confined along a κ curve. While we note some differences in the refraction characteristics from Fig. 7, it is clear that the horizontal wavelength and vertical velocity of the long-wave oscillation do not produce major changes in the refraction characteristics of these short waves. Note, however, that short-wave refraction is greater for $\zeta < 0$ than for $\zeta > 0$. In the former case, increases and decreases in k accentuate similar changes in ω, whereas for $\zeta > 0$, k tends to increase as ω decreases (and vice versa), which acts to reduce the range of short-wave refraction.

8. Effect of more than one long-wave oscillation

In all analysis up to this point, we have considered the refraction of short waves by a single long wave of constant steady amplitude. This yields a deterministic spreading of short-wave m and ω values. However, Doppler-spread theory considers the statistical properties of waves refracted by a randomly phased spectrum of many other waves. To study this to some extent, we consider a background field of linearly superposed long waves of the form

$$U_{lw}(x, z, t) = \sum_{i=1}^{J} (U_{max})_i \sin[(k_{lw})_i x + (m_{lw})_i z$$

$$- (\omega_{lw})_i t + (\vartheta_{lw})_i]$$

$$= \sum_{i=1}^{J} (U'_{lw})_i(x, z, t), \tag{36a}$$

$$V_{lw}(x, z, t) = \sum_{i=1}^{J} \left[\frac{-f}{(\omega_{lw})_i}\right] (U_{max})_i \cos[(k_{lw})_i x + (m_{lw})_i z$$

$$- (\omega_{lw})_i t + (\vartheta_{lw})_i], \tag{36b}$$

$$W_{lw}(x, z, t) = \sum_{i=1}^{J} \left[\frac{-(k_{lw})_i}{(m_{lw})_i}\right] (U'_{lw})_i(x, z, t), \tag{36c}$$

where the subscript i denotes the ith long-wave oscillation. The superposition is linear in that we have ignored any Doppler spreading of individual long-wave parameters or WKB violations that might arise as these long waves interact with each other. This is similar to the approach taken by Henyey and Pomphrey (1983) in their modeling of short-wave refraction in the ocean.

As a sample simulation of these effects, we selected $J = 8$ long waves and gave each one the same peak amplitude of $(U_{max})_i = 4$ m s^{-1}, which from (36a) and using the same m_c and N values as before, yields an rms β value of
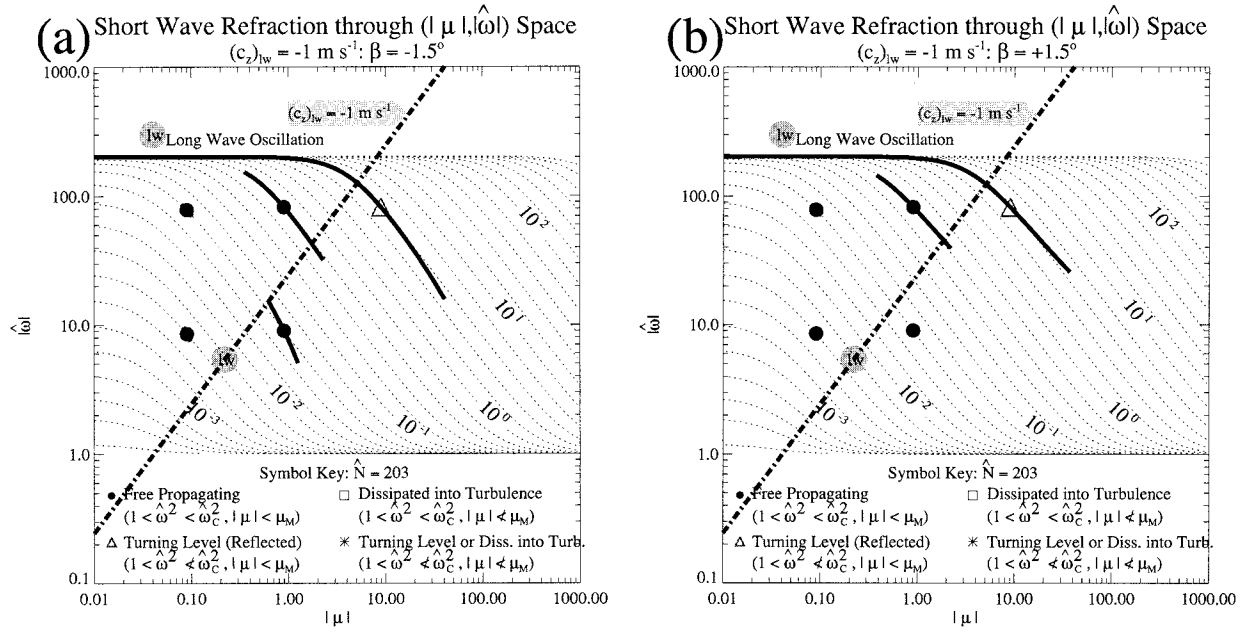
FIG. 9. As in Fig. 2 but using the short-wave solutions of section 4e assuming a long wave of $(c_z)_{lw} = -1$ m s^{-1} and (a) $\zeta = -1.5°$ and (b) $\zeta = +1.5°$. The critical-level criterion is replaced here with a dissipative criterion $|\mu| \geq \mu_M = 200$.

$$\beta_{rms} = \frac{(U_{lw})_{rms}m_c}{N} \approx 1. \qquad (37)$$

The locations of the eight long waves that we chose are shown in Fig. 10. We then traced short waves from $x_0 = z_0 = t_0 = 0$ through nine separate realizations of the superposed long-wave velocity field (36a)–(36c), changing the initial phases $(\vartheta_{lw})_i$ in each simulation. To match our earlier results as much as possible, we set $\mathbf{U}_{lw}(0, 0, 0) = 0$ so that the short wave always commenced propagation within a stationary atmosphere. This required choosing $(\vartheta_{lw})_i = n180°$, where n is a random integer. The short-wave ray equations were integrated using a 1 s time step.

Results for the five short waves considered earlier are shown in Fig. 10, for cases where $(k_{lw})_i < 0$ (panel a)
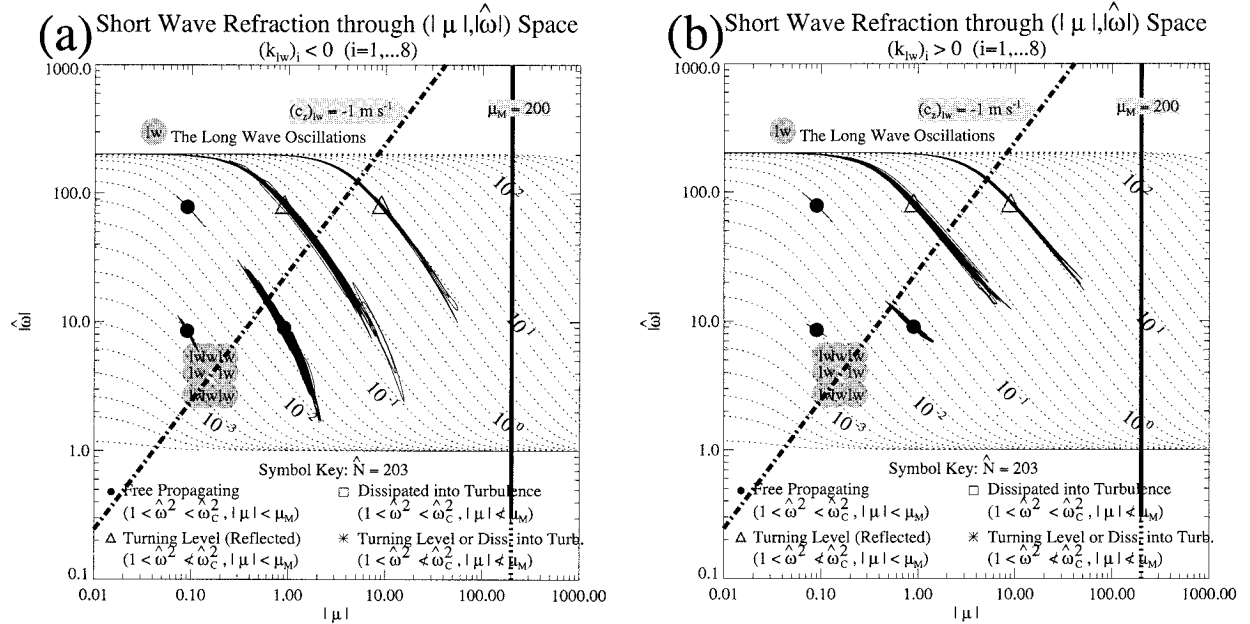

FIG. 10. As in Fig. 2 but showing for each short wave the results of nine separate numerical ray integrations through a field of eight superposed long-wave oscillations, for which (a) $(k_{lw})_i < 0$ and (b) $(k_{lw})_i > 0$. See section 8 for more details.
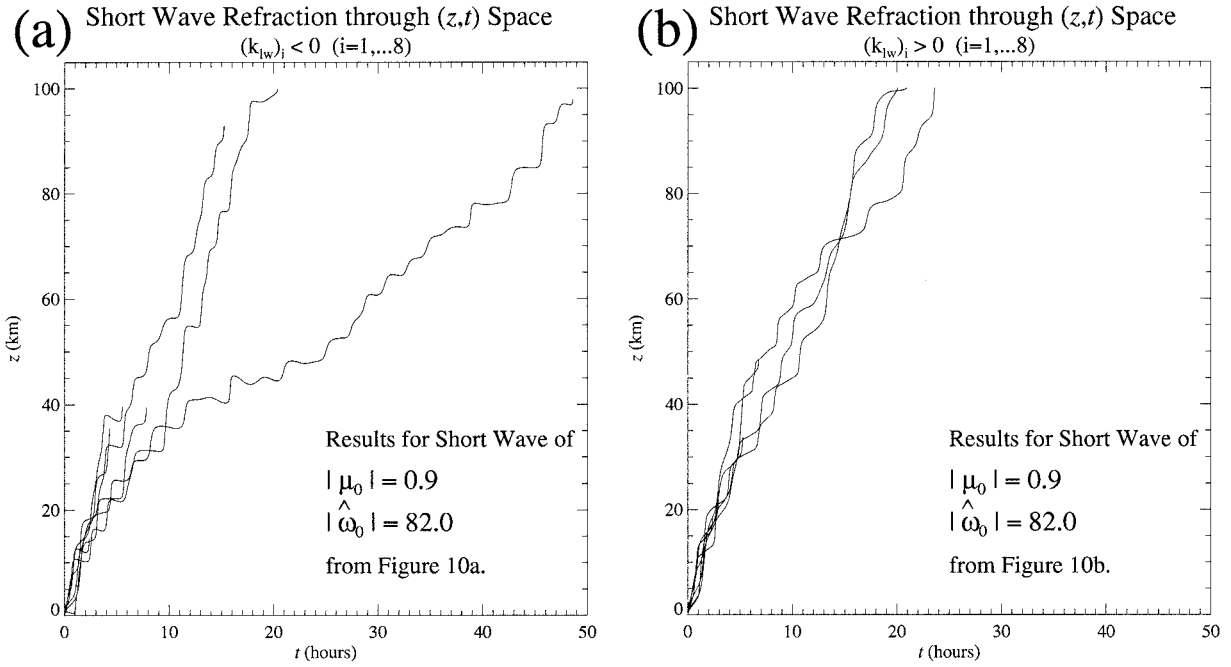
FIG. 11. Ray loci in (z, t) space from ray integrations for the short wave of initial parameters $|\mu_0| \approx 0.9$ and $|\hat{\omega}_0| \approx 82$ from Fig. 10, for the case (a) $(k_{lw})_i < 0$ (Fig. 10a) and (b) $(k_{lw})_i > 0$ (Fig. 10b). Rays that terminated before $z = 100$ km encountered turning levels.

and $(k_{lw})_i > 0$ (panel b). Nine curves are plotted for each short wave (i.e., 45 curves in each panel), summarizing short-wave refraction within each of the nine realizations of the long-wave velocity field (36a)–(36c). In addition to turning levels, ray integrations were also terminated if the short wave propagated either to a height of 100 km or for a time exceeding ~2.66 days (~3.75 inertial periods). These limits allowed free-propagating short waves to propagate through a minimum of eight cycles of each long-wave oscillation, thus allowing a more statistical picture of the short-wave refraction to emerge.

The range of refraction in Fig. 10 is greater than in Figs. 7 and 9. This occurs because β values greater than unity can arise here as the individual long waves superpose ($\beta_{max} \approx 4$ in these experiments). Despite this, there were no occurences of either critical levels or $|\mu|$ values exceeding $\mu_M = 200$, although two of the five waves were refracted to turning levels in some integrations (see Fig. 11). As in Fig. 9, short-wave refraction was greater for $(k_{lw})_i < 0$ ($\zeta_i < 0$) than for $(k_{lw})_i > 0$. Indeed, the basic characteristics of the refraction in Fig. 10 do not differ greatly from those in Figs. 7 and 9. In particular, there is again no tendency for short waves at $|\mu_0| \gtrsim 1$ to be removed via refraction to small vertical scales ($|\mu| > \mu_M$).

Time–height group trajectories for the short wave of $|\mu_0| \approx 0.9$ and $|\hat{\omega}_0| \approx 82$ from Fig. 10 are shown in Fig. 11. Note that in the $(k_{lw})_i < 0$ simulations (Fig. 11a), the short-wave group sometimes moves downward for a time. That the wave remains free propagating in these instances can be understood from the ray equation

$$\frac{dz}{dt} = c_{gz}^{gnd}(x, z, t) = W_{lw}(x, z, t) + c_{gz}(x, z, t), \quad (38)$$

where $c_{gz}^{gnd}(x, z, t)$ is the ground-based vertical group velocity of the wave. Instances of downward group motion in Fig. 11a occur when $W_{lw}(x, z, t) < c_{gz}^{gnd}(x, z, t) < 0$ so that the intrinsic frame is moving downward and the intrinsic group velocity remains upward ($c_{gz}(x, z, t) > 0$).

9. Validity of WKB ray theory (Approximation 2)

We have made extensive use of ray theory in sections 4–8, which requires that WKB plane-wave solutions for the short waves remain valid (i.e., that Approximation 2 always holds). We ensured this initially for the short waves using the longness criterion of section 3c. Here we briefly address the applicability of WKB ray theory for short waves within propagating long-wave fields.

For ray theory to remain valid within arbitrary environments, changes in wavenumber and frequency must always be much slower than the phase variations of the wave motion itself. Dimensionless parameters have been derived that check whether these conditions hold and can be evaluated at each time step during ray integrations (e.g., Einaudi and Hines 1970; Broutman 1984; Eckermann and Marks 1996). The results show that, typically, ray theory only breaks down at caustics (e.g., Broutman and Young 1986) or when the long-wave shear is so strong that it produces gradient Richardson numbers $\lesssim 1$ (Broutman 1984). In the scale-separated ray simulations reported here, WKB requirements

were violated and ray theory failed only as waves approached critical levels and turning levels, at which point we terminated further tracing of the ray. Elsewhere, approximation 2 remained valid. Thus, while we have demonstrated limited validity for approximation 1 in this study, approximation 2 is much more robust, giving us confidence that WKB ray methods can provide further insights into aspects of wave–wave interactions and wave spectra (e.g., Flatté et al. 1985; Henyey et al. 1986).

10. Discussion

The idealized problems in this paper were devised to provide insights into the range of validity of Approximations 1–3 of Doppler-spread theory, as well as interactions among atmospheric gravity waves in general. Critical scrutiny of these approximations was anticipated in two recent review articles by Hines (1996, 1997c). In these articles, Doppler-spread theory was cast within the broad general framework of advective nonlinearity, with mathematical development minimized to deflect criticisms of the theory based on the approximations used in earlier studies. Thus, potential ramifications of the present results for Doppler-spread theory have been anticipated to some extent and preemptively rebutted by Hines (1996, 1997c).

For example, Doppler-spread theory used Approximations 1–3 to derive model spectra of relative potential-temperature fluctuations at large Fourier wavenumbers M that asymptoted to M^{-1} shapes for $f = 0$ (see appendix B), as opposed to the observed M^{-3} shape. Hines (1993b, 1997c) argued that this breakdown in the theory at large M arose due to the onset of nonnegligible spreading by wave-induced vertical-velocity fluctuations (i.e., Approximation 1a broke down) but that Doppler-spread theory gave acceptable results for waves of intermediate $|m|$ values up to $\sim 10 \, m_c$. Derived spectra in this range had shapes close to M^{-3} at $M > M_c \sim m_c$.

Our scale-separated simulations indicated that it was Approximation 1b—the neglect of time variations of the background wave field—that broke down most notably at large $|m|$. Furthermore, it failed not just for large $|m|$ waves, but for all but the smallest $|m|$ (fastest c_{gz}) waves (see Fig. 6). When Approximation 1b was removed for the specific case of a short wave propagating through a long-wave background, any tendency for a sharp increase in the probability of short-wave obliteration at $|\mu_0| \gtrsim 1$ ($|m| \sim m_c$) was eliminated. Extensions of this model to include horizontal wavelengths (i.e., removal of approximation 1c), vertical-velocity fluctuations (removal of approximation 1a), and a background containing more than one long wave did not lead to any major changes in these basic conclusions.

The imposition of scale separation was critiqued by Hines (1997c) because spreading is produced only by long waves and so additional spreading by waves of similar or shorter spatial scales is omitted. Spreading by waves of all scales is permitted within Doppler-spread theory. While this of course is a valid criticism, scale separation was imposed here to ensure consistency with Approximations 1–2 of the original theory of Hines (1991b, 1993b). The view taken here is that these scale-separated simulations represent a proper application and extension of the original equations of Hines (1991b, 1993b) to a restricted class of interactions to which they are applicable. These simulations supported the basic contention of Doppler-spread theory that gravity wave m values are spread more as one progresses to larger $|m_0|$ values (e.g., Figs. 7, 9, and 10), and culminated in section 8 with numerical simulations that resembled the approach taken by Henyey and Pomphrey (1983) to model oceanic wave interactions.

Thus, while Doppler-spread theory is conceived to be a comprehensive model of broadband nonlinear advective processes, we view its current mathematical formulations as a simplified version of the "eikonal" (ray tracing) spectral models of oceanic gravity waves (e.g., Flatté et al. 1985; Henyey et al. 1986; Broutman et al. 1997). Hines (1991b, 1996, 1997c), on the other hand, argued that Doppler-spread theory corresponded best to "case III" of a general statistical mechanical theory of oceanic gravity waves developed by Allen and Joseph (1989). This model is discussed extensively by Hines (1991b, 1993b, 1996, 1997c), and an atmospheric version of it was presented recently by Chunchuzov (1996). Hines (1991b, 1997c) argued that the Allen and Joseph (AJ) model represented a full formal embodiment of Doppler-spread interactions, and he deferred to its findings at $M \gg M_c$, where it produced the required M^{-3} spectrum. Hines (1996, 1997c) further argued that the Doppler-spread theory of Hines (1991b, 1993b) complemented the AJ model by explaining physically both the formation of wavenumber cutoffs and the initial transition to decaying "tail spectra" at scales smaller than the cutoff wavenumbers.

However, the AJ model differs from eikonal models. It does not include refraction, but instead tracks the velocities and displacements of air parcels under the influence of a prescribed canonical distribution of wave modes. These Lagrangian displacements and velocities are then transformed to Eulerian measurement frames, and spectra are computed. While no modes exist at wavenumbers $|m| > \tilde{m}_c$ (where $\tilde{m}_c$ is the Lagrangian cutoff wavenumber), advective nonlinearities within the Eulerian frame produce variance at $M \gg M_c \sim \tilde{m}_c$ with an M^{-3} spectrum. This variance departs from the gravity-wave dispersion surface and so is considered to be nonwavelike and essentially devoid of physical significance when viewed from the Eulerian frame (Allen and Joseph 1989): Hines (1996, 1997c) has coined the term "wavulence" to describe it.

Conversely, no violations of the dispersion relation occur for waves in an eikonal formulation within the Eulerian frame: the system always remains entirely wavelike (Approximation 2), even as waves are refract-

ed to larger $|m|$ values to produce tail spectra. Allen and Joseph (1989) discuss other possible differences between their theory and eikonal theories on p. 216 of their paper (while noting that precise relationships between them are unclear). Given that the Doppler-spread formulation of Hines (1991b, 1993b) is viewed here as being a simplified eikonal formulation, then the degree to which Doppler-spread theory corresponds to the AJ model is unclear at present.

While Doppler-spread theory now defers to the AJ model in many areas, the original formulation of Hines (1991b, 1993b) is still used to predict the cutoff wavenumber m_c. This cutoff is a primary parameter in recent Doppler-spread parameterizations of gravity-wave momentum deposition (Hines 1997a, 1997b), yet no clear cutoff occurred in our scale-separated simulations once Approximation 1b was eliminated (see Fig. 8). If Doppler-spreading processes do produce a cutoff at $M \sim M_c$ and M^{-3} spectra thereafter, as argued by Hines (1991b, 1993b), then it seems that further extensions and refinements of the theory are needed to explain this result self-consistently.

Many important effects were omitted from our simulations. For example, we did not incorporate vertical profiles of mean wind velocities $\overline{U}(z)$, which refract waves appreciably as they propagate through the middle atmosphere in a manner consistent with the theory of sections 2 and 3 (e.g., Lindzen 1981; Eckermann 1995). Other important omissions include wave-induced thermal gradients, different horizontal propagation azimuths, damping, and saturation. While these processes can be incorporated within ray-based simulations (e.g., Marks and Eckermann 1995; Eckermann and Marks 1996), others cannot, such as strongly nonlinear non-scale-separated wave–wave and wave–turbulence interactions (e.g. Frederiksen and Bell 1984; Müller et al. 1986; Allen and Joseph 1989; Weinstock 1990; Sonmor and Klaassen 1996).

The experience gained from oceanic and laboratory studies may aid further understanding of atmospheric gravity wave interactions and spectra. The oceanic review of Müller et al. (1986) specifically recommended direct nonlinear numerical simulations of the oceanic wave field, and models of this kind have produced spectra in good agreement with observations (e.g., Orlanski and Cerasoli 1981; Shen and Holloway 1986; Hibiya et al. 1996). Recent numerical and laboratory experiments have also generated M^{-3} spectra as gravity waves become unstable and break (Benielli and Sommeria 1996; Bouruet-Aubertot et al. 1996), and wave overturning also observed by Shen and Holloway (1986) within their numerically simulated $\mathcal{K}^{-3}$ spectral regime. These issues relate to Approximation 3 of Doppler-spread theory, which we have said little about here, and merit further investigation in the atmosphere where wave dissipation is large. Similar models of atmospheric gravity wave spectra are still very limited (Frederiksen and Bell 1984; Huang et al. 1992) but are now feasible using existing codes and computing capabilities (e.g., Fritts et al. 1996).

11. Conclusions

In this study, we assessed key approximations used in Doppler-spread models of atmospheric gravity waves. Our results confirmed that the velocity oscillations of long waves produce important refractive spreading of short-wave vertical wavenumbers and frequencies in the atmosphere. However, we found that Doppler-spread models of these effects, which ignore the propagation of the long-wave velocity field, did not adequately describe either the amplitudes or group trajectories of short waves as they were refracted to shorter vertical wavelengths. We employed ray methods to describe more accurately the refraction and amplitude characteristics of short waves propagating through long waves. These solutions revealed a considerable reduction in the amount of wavenumber spreading compared to Doppler-spread predictions. Most notably, a cutoff in unspread vertical wavenumbers at $|m_0| \sim m_c$ ($|\mu_0| \sim 1$), which is a key aspect of Doppler-spread models of gravity-wave fluctuation spectra and momentum deposition, no longer occurred.

The simulations reported here dealt with a restricted and idealized class of advective wave–wave interactions. Nevertheless, the results indicated that more work is needed to understand the manner by and extent to which Doppler-spread-like processes influence the spectra and momentum dissipation of gravity waves within the atmosphere.

APPENDIX A

Gravity Wave Propagation through a Nonhorizontal Shear Flow

Here we consider gravity wave propagation through a stationary nonhorizontal zonally symmetric mean-flow profile $(U(z), 0, W(z))$, In the midfrequency approximation, a gravity wave propagating through such a region must satisfy the dispersion relation

$$\omega(z) = \Omega - kU(z) - m(z)W(z)$$

$$= k[c_x - U(z)] - m(z)W(z) = -\frac{kN}{m(z)}, \quad \text{(A1)}$$

for constant N and small curvature in the flow profile. Equation (A1) was used by Hines (1991b, 1993b) to gauge the effect that random U and W oscillations of larger-scale waves might have on the Doppler spreading of shorter waves. Hines (1991b) noted that (A1) produced a quadratic equation for m. Our purpose here is to highlight some interesting physical consequences of these solutions.

First, note that (A1) has the same basic form as (30), except that here $-W(z)$ appears in place of $(c_z)_{lw}$ and Ω appears in place of Ω'' (note also that Ω and Ω'' are both constants). Hence, from (31), the solution of (A1) is

$$m = \frac{1}{2W}\{k(c_x - U) \pm [k^2(c_x - U)^2 + 4kNW]^{1/2}\}.$$

$$(A2)$$

The solution of the wave action equation (11) is

$$(c_{gz} + W)A = \text{const}, \qquad (A3)$$

which again has the same form as (27) but with $(c_z)_{lw}$ replaced by $-W(z)$. Thus, the effects discussed in section 5 for the short-wave solutions (27) and (31) can also be applied to this problem.

For $W(z) > 0$, the solutions have the properties discussed in sections 5a and 5b. Thus critical levels vanish, and the amount of wavenumber–frequency refraction is reduced. Note in particular that when $c_x - U$ vanishes (the standard critical-level criterion for $W = 0$), then, from (A1) and (A2), the wave survives and has a vertical wavenumber $m = m_r$ and frequency $\omega = -m_r W$, where

$$m_r = - \left|\frac{kN}{W}\right|^{1/2}. \qquad (A4)$$

The case $W(z) < 0$ has much in common with the antipropagating solutions discussed in section 5c. No solutions for m are possible when the discriminant in (A2) is negative. This also occurs at $m = m_r$, which in this case corresponds to the condition

$$c_{gz} = -W. \qquad (A5)$$

This, in turn, yields $A \to \infty$ according to (A3), which is a caustic singularity equivalent to the one studied by Broutman and Young (1986). The explosive buildup of wave action density near these caustic points implied by (A5) and (A3) suggests that wave saturation may be possible, depending on the initial amplitude of the wave (see also Broutman 1986; Broutman et al. 1997). WKB conditions break down in these regions, and Broutman and Young (1986) argued that "separatrix crossings" occur at the caustic point, which correspond to a transfer from one root to the other in (A2), an assertion supported in later studies by Broutman (1986) and Bruhwiler and Kaper (1995). The caustic ($m = m_r$) occurs at an intrinsic horizontal phase speed of

$$|(c_x - U)_r| = 2\left|\frac{m_r W}{k}\right| = 2\left|\frac{NW}{k}\right|^{1/2}. \qquad (A6)$$
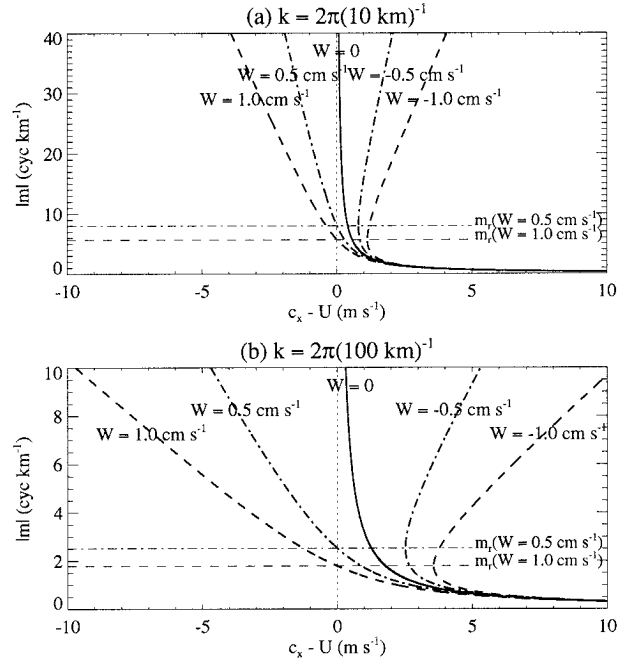

FIG. A1. Loci of intrinsic horizontal phase speeds $|c_x - U|$ and vertical wavenumbers $|m|$ for a gravity wave in the presence of five different values of W, as labeled on each curve. Results are shown for (a) $k = 2\pi (10 \text{ km})^{-1}$ and (b) $k = 2\pi (100 \text{ km})^{-1}$. See text for further details.

Thus, for $W \neq 0$, the "critical level" criterion $|c_x - U| = 0$ can be replaced by a more general "caustic level" criterion $c_{gz} + W = 0$ implied by (A3) and (A5). The critical level then follows as a limiting form of the caustic-level condition as c_{gz} and W both approach zero.

Figure A1 shows the variation of $|m|$ as a function of $c_x - U$ for various values of W and k. The turning points on the $W < 0$ curves correspond to the caustic point, as defined by (A4) and (A6), and demark where the solutions cross from one of the roots in (A2) to the other. Note too that the $W > 0$ curves yield $m = m_r$ at $c_x - U = 0$.

APPENDIX B

Asymptotic "Doppler Spread" Spectra at Large M

Hines (1991b) considered the power spectrum of relative fluctuations in potential temperature, $\Theta^2(k, m)$. Approximations 1 and 2, which use "fast limit" solutions (see section 5a), yielded a spectral conservation relation (e.g. Hines 1991b)

$$\Theta^2(k, m) = \Theta_0^2(k, m_0)\frac{m}{m_0}\frac{dm_0}{dm}. \qquad (B1)$$

This arises from conservation of B_z with height for short-wave solutions in the fast limit. Hines used midfrequency approximations, which, from (5), yield $dm_0/dm = (m_0/m)^2$, so (B1) becomes

$$\Theta^2(k, m) = \Theta_0^2(k, m_0)m_0 m^{-1}. \qquad (B2)$$

From here, Hines (1991b) used statistical methods to describe the multiwave Doppler spreading of short-wave m values by larger-scale waves using probability density functions, which he integrated through the right hand side of (B2) using models of $\Theta_0^2(k, m_0)$ to yield a one-dimensional model Doppler-spread spectrum $\Theta^2(M)$. The m^{-1} factor in (29) carried through this integration and ultimately yielded an asymptotic M^{-1} dependence of the spectrum at $M \gg M_C$ (where $M_C = N/2\sigma_T$ in his derivation and σ_T is the total horizontal velocity variance of the wave field).

We can rework this analysis using the $\zeta = 0$ short-wave solutions in the midfrequency approximation. Since in this particular problem nondissipating short waves conserve $-(c_z)_{lw}A(r + 1)$ from (33), where $A = E/\omega \approx -Em/kN$, and $k, N,$ and $(c_z)_{lw}$ are constants, then this implies

$$\Theta^2(k, m) = \Theta_0^2(k, m_0)\frac{m_0(1 + r_0)}{m(1 + r)}\frac{dm_0}{dm}, \qquad (B3)$$

where r_0 is the phase/group ratio at m_0. Combining (30) and (35) to eliminate frequency terms, and then differentiating, yields

$$\frac{dm_0}{dm} = \frac{1 + r}{1 + r_0}. \qquad (B4)$$

Substitution of (B4) into (B3) then yields the same result as (B2) and, hence, the same asymptotic M^{-1} spectral shape at large Fourier wavenumbers M. Note that this derivation holds only for a short wave propagating though a single low-frequency ($\zeta \approx 0$) long wave of constant amplitude in an unsheared mean flow.

REFERENCES

Allen, K. R., and R. I. Joseph, 1989: A canonical statistical theory of oceanic internal waves. *J. Fluid Mech.,* **204,** 185–228.

Allen, S. J., and R. A. Vincent, 1995: Gravity-wave activity in the lower atmosphere: Seasonal and latitudinal variations. *J. Geophys. Res.,* **100,** 1327–1350.

Andrews, D. G., and M. E. McIntyre, 1978: On wave-action and its relatives. *J. Fluid Mech.,* **89,** 647–664.

Bacmeister, J. T., S. D. Eckermann, P. A. Newman, L. Lait, K. R. Chan, M. Loewenstein, M. H. Profitt, and B. L. Gary, 1996: Stratospheric horizontal wavenumber spectra of winds, potential temperature and atmospheric tracers observed by high-altitude aircraft. *J. Geophys. Res.,* **101,** 9441–9470.

Benielli, D., and J. Sommeria, 1996: Excitation of internal waves and stratified turbulence by parametric instability. *Dyn. Atmos. Oceans,* **23,** 335–343.

Bouruet-Aubertot, P., J. Sommeria, and C. Staquet, 1996: Stratified turbulence produced by internal wave breaking: Two-dimensional numerical experiments. *Dyn. Atmos. Oceans,* **23,** 357–369.

Broutman, D., 1984: The focusing of short internal waves by an inertial wave. *Geophys. Astrophys. Fluid Dyn.,* **30,** 199–225.

——, 1986: On internal wave caustics. *J. Phys. Oceanogr.,* **16,** 1625–1635.

——, and W. R. Young, 1986: On the interaction of small-scale in-

ternal waves with near-inertial waves. *J. Fluid Mech.,* **166,** 341–358.

——, C. Macaskill, M. E. McIntyre, and J. W. Rottman, 1997: On Doppler-spreading models of internal waves. Preprints, *11th Conf. on Atmospheric and Oceanic Fluid Dynamics,* Tacoma, WA, Amer. Meteor. Soc., 304–308.

Bruhwiler, D. L., and T. J. Kaper, 1995: Wavenumber transport: Scattering of small-scale internal waves by large-scale wavepackets. *J. Fluid Mech.,* **289,** 379–405.

Chunchuzov, I. P., 1996: The spectrum of high-frequency internal waves in the atmospheric waveguide. *J. Atmos. Sci.,* **53,** 1798–1814.

D'Asaro, E. A., and M. D. Morehead, 1991: Internal waves and velocity fine structure in the Arctic Ocean. *J. Geophys. Res.,* **96,** 12 725–12 738.

Desaubies, Y., and W. K. Smith, 1982: Statistics of Richardson number and instability in oceanic internal waves. *J. Phys. Oceanogr.,* **12,** 1245–1259.

Dewan, E. M., 1991: Similitude modeling of internal gravity wave spectra. *Geophys. Res. Lett.,* **18,** 1473–1476.

——, and R. E. Good, 1986: Saturation and the "universal" spectrum for vertical profiles of horizontal scalar winds in the atmosphere. *J. Geophys. Res.,* **91,** 2742–2748.

Eckermann, S. D., 1992: Ray-tracing simulation of the global propagation of inertia gravity waves through the zonally-averaged middle atmosphere. *J. Geophys. Res.,* **97,** 15 849–15 866.

——, 1995: Effect of background winds on vertical wavenumber spectra of atmospheric gravity waves. *J. Geophys. Res.,* **100,** 14 097–14 112.

——, and C. J. Marks, 1996: An idealized ray model of gravity wave–tidal interactions. *J. Geophys. Res.,* **101,** 21 195–21 212.

——, I. Hirota, and W. K. Hocking, 1995: Gravity wave and equatorial wave morphology of the stratosphere derived from long-term rocket soundings. *Quart. J. Roy. Meteor. Soc.,* **121,** 149–186.

Einaudi, F., and C. O. Hines, 1970: WKB approximation in application to acoustic-gravity waves. *Can. J. Phys.,* **48,** 1458–1471.

Flatté, S. M., F. S. Henyey, and J. A. Wright, 1985: Eikonal calculations of short-wavelength internal-wave spectra. *J. Geophys. Res.,* **90,** 7265–7272.

Frederiksen, J. S., and R. C. Bell, 1984: Energy and entropy evolution of interacting gravity waves and turbulence. *Geophys. Astrophys. Fluid Dyn.,* **28,** 171–203.

Fritts, D. C., and T. E. VanZandt, 1987: Effects of Doppler shifting on the frequency spectra of atmospheric gravity waves. *J. Geophys. Res.,* **92,** 9723–9732.

——, and L. Yuan, 1989: An analysis of gravity wave ducting in the atmosphere: Eckart's resonances in thermal and Doppler ducts. *J. Geophys. Res.,* **94,** 18 455–18 466.

——, and W. Lu, 1993: Spectral estimates of gravity wave energy and momentum fluxes. Part II: Parameterization of wave forcing and variability. *J. Atmos. Sci.,* **50,** 3695–3713.

——, J. F. Garten, and Ø. Andreassen, 1996: Wave breaking and transition to turbulence in stratified shear flows. *J. Atmos. Sci.,* **53,** 1057–1085.

Gardner, C. S., 1994: Diffusive filtering theory of gravity wave spectra in the atmosphere. *J. Geophys. Res.,* **99,** 20 601–20 622.

——, C. A. Hostetler, and S. Lintelman, 1993: Influence of the mean wind field on the separability of atmospheric perturbation spectra. *J. Geophys. Res.,* **98,** 8859–8872.

Gossard, E. E., and W. H. Hooke, 1975: *Waves in the Atmosphere.* Elsevier Science, 456 pp.

Grimshaw, R., 1984: Wave action and wave–mean flow interaction, with applications to stratified shear flows. *Annu. Rev. Fluid Mech.,* **16,** 11–44.

Henyey, F. S., and N. Pomphrey, 1983: Eikonal description of internal wave interactions: A non diffusive picture of "induced diffusion." *Dyn. Atmos. Oceans,* **7,** 189–219.

——, J. Wright, and S. M. Flatté, 1986: Energy and action flow

through the internal wave field: An eikonal approach. *J. Geophys. Res.,* **91,** 8487–8495.

Hibiya, T., Y. Niwa, K. Nakajima, and N. Suginohara, 1996: Direct numerical simulation of the roll-off range of internal wave shear spectra in the ocean. *J. Geophys. Res.,* **101,** 14 123–14 129.

Hines, C. O., 1991a: The saturation of gravity waves in the middle atmosphere. Part I: Critique of linear-instability theory. *J. Atmos. Sci.,* **48,** 1348–1359.

——, 1991b: The saturation of gravity waves in the middle atmosphere. Part II: Development of Doppler-spread theory. *J. Atmos. Sci.,* **48,** 1360–1379.

——, 1991c: The saturation of gravity waves in the middle atmosphere. Part III: Formation of the turbopause and of the turbulent layers beneath it. *J. Atmos. Sci.,* **48,** 1380–1385.

——, 1993a: Pseudosaturation of gravity waves in the middle atmosphere: An interpretation of certain lidar observations. *J. Atmos. Terr. Phys.,* **55,** 441–445.

——, 1993b: The saturation of gravity waves in the middle atmosphere. Part IV: Cutoff of the incident wave spectrum. *J. Atmos. Sci.,* **50,** 3045–3060.

——, 1996: Nonlinearity of gravity wave saturated spectra in the middle atmosphere. *Geophys. Res. Lett.,* **23,** 3309–3312.

——, 1997a: Doppler-spread parameterization of gravity-wave momentum deposition in the middle atmosphere. Part 1: Basic formulation. *J. Atmos. Terr. Phys.,* **59,** 371–386.

——, 1997b: Doppler-spread parameterization of gravity-wave momentum deposition in the middle atmosphere. Part 2: Broad spectra and quasi monochromatic waves, and implementation. *J. Atmos. Terr. Phys.,* **59,** 387–400.

——, 1997c: Nonlinearity of the saturation spectrum. *Gravity Wave Processes: Their Parameterization in Global Models,* K. Hamilton, Ed., NATO ASI Series, Vol. I 50, Springer-Verlag, 227–244.

Hirota, I., and T. Niki, 1985: A statistical study of inertia-gravity waves in the middle atmosphere. *J. Meteor. Soc. Japan,* **63,** 1055–1066.

Holloway, G., 1980: Oceanic internal waves are not weak waves. *J. Phys. Oceanogr.,* **10,** 906–914.

Huang, C. M., F. S. Kuo, H. Y. Lue, and C. H. Liu, 1992: Numerical simulations of the saturated gravity wave spectra in the atmosphere. *J. Atmos. Terr. Phys.,* **54,** 129–142.

Jones, W. L., 1967: Propagation of internal gravity waves in fluids with shear flow and rotation. *J. Fluid Mech.,* **30,** 439–448.

——, 1969: Ray tracing for internal gravity waves. *J. Geophys. Res.,* **74,** 2028–2033.

Lawrence, B. N., 1997: The effect of parameterized gravity wave drag on simulations of the middle atmosphere during northern winter 1991/92—General evolution. *Gravity Wave Processes: Their Parameterization in Global Models,* K. Hamilton, Ed., NATO ASI Series, Vol. I 50, Springer-Verlag, 291–307.

Lindzen, R. S., 1981: Turbulence and stress owing to gravity wave and tidal breakdown. *J. Geophys. Res.,* **86,** 9707–9714.

Manzini, E., N. A. McFarlane, and C. McLandress, 1997: Middle atmosphere simulations with the ECHAM4 model: Sensitivity

to the Doppler-spread parameterization. *Gravity Wave Processes: Their Parameterization in Global Models,* K. Hamilton, Ed., NATO ASI Series, Vol. I 50, Springer-Verlag, 367–381.

Marks, C. J., and S. D. Eckermann, 1995: A three-dimensional non-hydrostatic ray-tracing model for gravity waves: Formulation and preliminary results for the middle atmosphere. *J. Atmos. Sci.,* **52,** 1959–1984.

McComas, C. H., and F. P. Bretherton, 1977: Resonant interaction of oceanic internal waves. *J. Geophys. Res.,* **82,** 1397–1412.

Medvedev, A. S., and G. P. Klaassen, 1995: Vertical evolution of gravity wave spectra and the parameterization of associated wave drag. *J. Geophys. Res.,* **100,** 25 841–25 853.

Mengel, J. H., H. G. Mayr, K. L. Chan, C. O. Hines, C. A. Reddy, N. F. Arnold, and S. F. Porter, 1995: Equatorial oscillations in the middle atmosphere generated by small-scale gravity waves. *Geophys. Res. Lett.,* **22,** 3027–3030.

Müller, P., G. Holloway, F. S. Henyey, and N. Pomphrey, 1986: Nonlinear interactions among internal gravity waves. *Rev. Geophys.,* **24,** 493–536.

Munk, W., 1981: Internal waves and small-scale processes. *Evolution of Physical Oceanography,* B. A. Warren and C. Wunsch, Eds., The MIT Press, 264–291.

Orlanski, I., and C. P. Cerasoli, 1981: Energy transfer among internal gravity modes: Weak and strong interactions. *J. Geophys. Res.,* **86,** 4103–4124.

Schoeberl, M. R., 1985: A ray-tracing model of gravity wave propagation and breakdown in the middle atmosphere. *J. Geophys. Res.,* **90,** 7999–8010.

Shen, C. Y., and G. Holloway, 1986: A numerical study of the frequency and the energetics of nonlinear internal gravity waves. *J. Geophys. Res.,* **91,** 953–973.

Sherman, J. T., and R. Pinkel, 1991: Estimates of the vertical wavenumber-frequency spectra of vertical shear and strain. *J. Phys. Oceanogr.,* **21,** 292–303.

Smith, S. A., D. C. Fritts, and T. E. VanZandt, 1987: Evidence for a saturated spectrum of atmospheric gravity waves. *J. Atmos. Sci.,* **44,** 1404–1410.

Sonmor, L. J., and G. P. Klaassen, 1996: Higher-order resonant instabilities of internal gravity waves. *J. Fluid Mech.,* **324,** 1–23.

Thorpe, S. A., 1989: The distortion of short internal waves produced by a long wave, with application to ocean boundary mixing. *J. Fluid Mech.,* **208,** 395–415.

Tsuda, T., T. E. VanZandt, M. Mizumoto, S. Kato, and S. Fukao, 1991: Spectral analysis of temperature and Brunt–Väisälä frequency fluctuations observed by radiosondes. *J. Geophys. Res.,* **96,** 17 265–17 278.

Weinstock, J., 1990: Saturated and unsaturated spectra of gravity waves, and scale-dependent diffusion. *J. Atmos. Sci.,* **47,** 2211–2225.

Zhong, L., L. J. Sonmor, A. H. Manson, and C. E. Meek, 1995: The influence of time-dependent wind on gravity-wave propagation in the middle atmosphere. *Ann. Geophys.,* **13,** 375–394.

Zhu, X., 1994: A new theory of the saturated gravity wave spectrum for the middle atmosphere. *J. Atmos. Sci.,* **51,** 3615–3626.